using dynamic positron emission tomography. J Cereb Blood Flow Metab 1989;9:874–85.

[18] Magata Y, Temma T, Iida H, Ogawa M, Mukai T, Iida Y, et al. Development of injectable O-15 oxygen and estimation of rat OEF. J Cereb Blood Flow Metab 2003;23:671–6.

[19] Iida H, Kanno I, Miura S, Murakami M, Takahashi K, Uemura K. Error analysis of a quantitative cerebral blood flow measurement using $H_2^{15}O$ autoradiography and positron emission tomography, with respect to the dispersion of the input function. J Cereb Blood Flow Metab 1986;6(5):536–45.

[20] Iida H, Miura S, Shoji Y, Ogawa T, Kado H, Narita Y, et al. Noninvasive quantitation of cerebral blood flow using oxygen-15-water and a dual-PET system. J Nucl Med 1998;39(10):1789–98.

[21] Meyer PT, Circiumaru V, Cardi CA, Thomas DH, Bal H, Acton PD. Simplified quantification of small animal [^{18}F]FDG PET studies using a standard arterial input function. Eur J Nucl Med Mol Imaging 2006;33:948–54.

[22] Grubb RL, Raichle ME, Eichling JO, Ter-Pogossian MM. The effects of changes in $PaCO_2$ on cerebral blood volume, blood flow, and vascular mean transit time. Stroke 1974;5:630–9.

[23] White JC, Brooks JR, Goldthwait JC, Adams RD. Changes in brain volume and blood content after experimental concussion. Ann Surg 1943;118(4):619–33.

[24] James IM, Millar RA, Purves MJ. Observations on the extrinsic neural control of cerebral blood flow in the baboon. Circ Res 1969;25(1):77–93.

[25] Williams DS, Detre JA, Leigh JS, Koretsky AP. Magnetic resonance imaging of perfusion using spin inversion of arterial water. Proc Natl Acad Sci USA 1992;89:212–6.

[26] Kudomi N, Hayashi T, Teramoto N, Watabe H, Kawachi N, Ohta Y, et al. Rapid quantitative measurement of CMRO2 and CBF by dual administration of 15O-labeled oxygen and water during a single PET scan-a validation study and error analysis in anesthetized monkeys. J Cereb Blood Flow Metab 2005;25(9):1209–24.

Biomaterials 33 (2012) 2439–2448

Contents lists available at SciVerse ScienceDirect

Biomaterials

journal homepage: www.elsevier.com/locate/biomaterials

The use of magnetic resonance cell tracking to monitor endothelial progenitor cells in a rat hindlimb ischemic model

Carlos A. Agudelo [a], Yoichi Tachibana [b], Andres F. Hurtado [a], Takayuki Ose [b], Hidehiro Iida [b], Tetsuji Yamaoka [a,*]

[a] Department of Biomedical Engineering, National Cardiovascular Center Research Institute, 5-7-1 Fujishiro-dai, Suita, Osaka 565-8565, Japan
[b] Department of Investigative Radiology Advanced Medical Engineering Center, National Cerebral and Cardiovascular Center Research Institute, 5-7-1 Fujishiro-dai, Suita, Osaka 565-8565, Japan

ARTICLE INFO

Article history:
Received 7 November 2011
Accepted 25 November 2011
Available online 27 December 2011

Keywords:
Dextran
MRI
Progenitor cell
Transplantation

ABSTRACT

A water-soluble magnetic resonance imaging (MRI) contrast agent, Dextran mono-N-succinimidyl 1,4,7,10-tetraazacyclododecane-1,4,7,10-tetraacetate-gadolinium^{3+} (Dex-DOTA-Gd^{3+}), was shown to enable monitoring of the anatomical migration and the survival period of transplanted stem cells for up to 1 month. Gadolinium molecules in the cells were rapidly eliminated from the site and excreted upon cell death. Endothelial progenitor cells (EPCs) transplanted into the inguinal femoral muscle of rats migrated distally through the knee in rats after hindlimb ischemia but did not migrate in non-ischemic rats. Interestingly, the survival period of transplanted EPCs was notably prolonged in the ischemic limb, indicating that EPCs are required by the ischemic tissues and that the fate of transplanted EPCs was affected by the disease. Compared to the commonly used particle type of MRI contrast agents, the system described in this study is expected to be invaluable to help clarifying the process of stem cell transplantation therapy.

1. Introduction

In the last decades, transplantation of hematopoietic stem cells, bone marrow (BM)-derived mesenchymal stem cells, and adipose tissue-derived mesenchymal stem cells has been reported to stimulate regeneration of different tissues such as ischemic limb [1–6], ischemic myocardium [7–9], and brain [10]. Endothelial progenitor cells (EPCs), which are crucial in the regeneration of injured tissues and organs, act through a molecular mechanism known as angiogenesis [10,11]. This post-natal revascularization starts with the recruitment of EPCs from stem cell reservoirs such as BM [12,13]. According to the paradigm of angiogenesis, EPC transplantation may offer a source of feasible endothelial cells that migrate and proliferate from preexisting blood vessels, thus promoting revascularization in the ischemic limb, contributing to angiogenesis [10,14]. Although the mechanisms of homing and differentiation of EPCs are not well understood, tissue ischemia results in the upregulation of several angiogenic factors such as vascular endothelial growth factor (VEGF), which interacts with 2 tyrosine kinase receptors, VEGF receptor-2 (VEGF-R2 or fetal liver kinase 1 [Flk-1], kinase domain receptor [KDR]) and VEGF receptor-1 (VEGFR1, Flt-1), stromal cell-derived factor-1 (SDF-1), insulin-like growth factor-1 (IGF-1), and hepatocyte growth factor (HGF). These growth factors are all expressed in several cell types, including EPCs, that promote migration to the injury site [15,19]. However, some studies have shown that neovascularization of ischemic tissues may not be exclusively attributed to the incorporation of EPCs into the vessels, but also to paracrine effects that probably influence the process of angiogenesis by releasing pro-angiogenic factors [20,21].

The ability to noninvasively track cells in vivo and follow their location after transplantation would significantly contribute to our understanding of the effects of stem cell therapy. Magnetic resonance imaging (MRI) is one of the noninvasive methods employed to examine the migratory behavior of stem and progenitor cells based on its whole-body spatial resolution, even in three-dimensional images. In MRI cell tracking, contrast agents are used to improve the quality of an image or to label transplanted cells to facilitate the detection of their location within the tissue. The most commonly used contrast agents, which have been successfully employed in tracking a variety of cell lineages, are superparamagnetic iron oxide (SPIO) and its derivatives. Progenitor cells have been tracked in vitro by using Tat peptide-derived SPIO. The high contrast of SPIO-labeled cells allows imaging of a single cell [22]. Other studies have demonstrated the feasibility of imaging

* Corresponding author. Fax: +81 6 6835 5476.
E-mail address: yamtet@ri.ncvc.go.jp (T. Yamaoka).

0142-9612/$ – see front matter © 2011 Elsevier Ltd. All rights reserved.
doi:10.1016/j.biomaterials.2011.11.075

small quantities of SPIO-labeled cells using high-resolution MRI [23,24]. Bulte et al. reported in vivo tracking of migrating cells labeled with dextran-coated iron oxide in the brain parenchyma for about 32 days [24]. Long-term monitoring of SPIO-labeled cells has also been reported by Guzman et al. in transplanted human neural stem cells [25] and Hoehn et al. in embryonic stem cells [26].

Despite the high sensitivity and resolution of SPIO tracking of labeled stem cells in vivo, this method has some disadvantages. In one report, the MRI signal that was attributed to the transplanted stem cells was found to actually be produced by macrophages that had phagocytosed the iron particles. When tracking mesenchymal stem cells in infarcted myocardium, Amsalem et al. reported that the signal was generated by cardiac macrophages that engulfed SPIO [27]. This phenomenon was lately confirmed by Terrovitis et al., who also demonstrated that the MRI signal was generated by iron-loaded macrophages rather than iron-labeled stem cells [28].

In another study by Li et al. [29] tracking human embryonic stem cells and endothelial cells by using iron particles and reporter gene for tracking implanted cells into hind limbs, showed a discrepancy between the acquired MRI signal of cells, which persisted for 28 days post-transplantation, and the genetically introduced bioluminescent signal that progressively decreased within 2 weeks. Further histological analysis revealed that most of the iron particles were taken up by macrophages in the ischemic limb. In a recent report, Winter et al. demonstrated that iron oxide fails to distinguish dead from living transplanted cells in non-obese diabetic/severe combined immunodeficient mice [30].

These reports indicate that although this method is useful for tracking the anatomic location of labeled cells after direct implantation, it does not provide reliable information about cell fate in the long term.

We previously developed water-soluble polymeric gadolinium chelate contrast agents for labeling NIH-3T3 cells [31]. Since, water-soluble polymers behave very differently from the particulate materials [32,33], the problems with the SPIO was expected to be solved. We then recently selected dextrans (Dex) as biocompatible carriers [34] and succeeded to label BM-derived EPCs with Dextran-mono-N-succinimidyl 1,4,7,10-tetraazacyclododecane-1,4,7,10-tetraacetate-gadolinium^{3+} (Dex-DOTA-Gd^{3+}). Dex-DOTA-Gd^{3+} demonstrated the excellent capacity for ex vivo cell labeling before transplantation, a high intracellular stability, and biocompatibility without affecting cell viability and proliferation [35].

EPC transplantation therapy is of remarkable importance in the regeneration process of ischemic tissues. Therefore, there is a critical need to refine the techniques for visualization of EPC recruitment, homing, and migration that accompany the release of various cytokines, which is a process that needs to be studied more carefully.

If we hypothesize that living EPCs labeled with Dex-DOTA-Gd^{3+} can be tracked by MRI during their migration from the transplantation point to the foci of vascularization, the behavioral pattern of these cells in an ischemic limb should differ from that in a non-ischemic limb and also from the pattern exhibited by SPIO-labeled cells. We also challenged the quantification of cell survival by measuring the amount of excreted Gd on the basis of the feature of the contrast agent that will be probably released from dead cells and rapidly cleared from the body.

2. Materials and methods

2.1. Isolation of EPCs

All animal experiments were performed according to a protocol approved by our animal facility and use committee. BM was flushed from femurs and tibias of F344 rats (4 weeks old, male) after previous cytokine-induced mobilization of BM-derived EPCs by using granulocyte colony-stimulating factor (G-CSF, Kirin Pharma, Japan) (200 μg kg^{-1}·day^{-1} for 5 days, subcutaneously injected) [36]. CD34- and Flk-1-positive BM cells were isolated using magnetic beads (Streptavidin Microbeads, Miltenyi Biotec GmbH, Gladbach, Germany) coated with anti CD34 and Flk-1 antibodies (sc-6251 and sc-7324, Santa Cruz Biotechnology Inc., CA) and a Biotin Labeling kit-NH_2 (Dojindo Molecular Technologies Inc., Japan). Cells were placed in fibronectin-coated dishes and cultured with an endothelial cell basal medium (EBM-2) supplemented with endothelial growth medium 2 (EGM-2 SingleQuots, Clonetics Lonza, Walkersville, MD) [15].

2.2. Rat ischemic limb model

To investigate if Dex-DOTA-Gd^{3+} labeling may have any adverse effect on the neovascularization of a rat ischemic limb model, male F344 rats (8 weeks old) were anesthetized with isoflurane (1.5% in air). The left femoral artery and vein and their branches were ligated and completely excised through a skin incision [37]. Rats ($n = 6$) were injected in 3 places with a total of 150 μl of Bolheal® containing Dex-DOTA-Gd^{+3}-labeled EPCs [35]. Injections were applied as follows: to allow normal movement of the cells through the muscle, 6.3×10^6 labeled cells in 75 μl Bolheal® component A (thrombin, 250 unit/ml) were intramuscularly injected in 3 different places in the abductor and quadriceps (total $1.8–2 \times 10^7$ cells) and then, 75 μl Bolheal® component B (fibrinogen, 80 mg/ml) was injected in the same sites to temporarily immobilize the cells (gelation occurred in the muscle). Ischemic limb controls ($n = 6$) were injected with Bolheal® which did not contain cells.

2.3. Laser Doppler analysis

The ratio of the ischemic (left)/non-ischemic (right) limb blood flow was measured by using a Laser Doppler Perfusion Imager (LDPI; Moor Instruments Ltd., MoorLDI, Millwey, England). Blood flow was scanned twice and images were subjected to computer-assisted quantification. The average blood flow of ischemic and non-ischemic limbs was calculated.

2.4. Angiography

Angiograms were obtained 35 days after transplantation of Dex-DOTA-Gd^{3+}-labeled EPCs. Animals were anesthetized and a pig tail catheter was positioned in the distal abdominal aorta approximately 1.5 cm above the iliac bifurcation, and anteroposterior digital subtraction angiograms of the pelvis and both limbs were acquired at a film rate of 15 frames per second using a digital mobile imaging system (GE OEC 9800 system, GE OEC Salt Lake City, UT) (control rats: $n = 3$, EPC-transplanted rats: $n = 3$). Omnipaque-350 (iohexol) was injected at rate of 400 μl/s (total: 1.2 ml) [6].

2.5. MRI measurements

Dex-DOTA-Gd^{3+}-labeled EPCs were identified in vivo using T1-weighted images obtained with a 1.5-T compact MRI system (MRmini, Dainippon Sumitomo Pharma, Osaka, Japan) with a repetition time (TR) of 2000 ms and an echo time (TE) of 9 ms (field of view [FOV], 4 × 8 cm; matrix, 126 × 256; slice thickness, 1 mm; slice gap, 0 mm; number of slices, 35).

2.6. Gadolinium concentration in cells, organs, urine, and feces

To quantify the concentration of Gd(III) paramagnetic species in labeled EPCs, cells were placed in 60-mm dishes and cultured for 1 day. EPCs were electroporated as described in supplementary methods and then, detached, counted, and placed in 15-ml tubes. Samples were treated with nitric acid to measure the concentration of Gd by inductively coupled plasma atomic emission spectroscopy (ICP-AES, Model 8500, Shimadzu Co., Kyoto, Japan).

2.7. Statistical analysis

All data are expressed as means ± SD. Statistical significance was evaluated using an unpaired 2-tailed Student's *t test* for 2 variables. Differences were considered significant when P values were less than 0.05.

3. Results

3.1. Dex-DOTA-Gd^{3+}-labeled EPCs

BM-derived cells (passage 4-5) that incorporated lectin and DiI-acLDL are shown in Supplementary Fig. 1A–D, respectively. Double-positive cells (Supplementary Fig. 1E and F) were identified as EPCs [15,18,19]. Additional staining with eNOS was performed (Santa Cruz Biotechnology Inc., Santa Cruz, CA, 20 μg/ml, $n = 3$) at 37 °C for 4 h. BM-derived cells that were stained positive

for eNOS where confirmed to exhibit an endothelial phenotype [37,15].

The Impact of Dex-DOTA-Gd^{3+} labeling on the expression of four membrane proteins specific to the endothelial phenotype (Fig. 1E). In the same culture condition, tree different samples were analyzed on days 1 and 2 after labeling by electroporation. PECAM-1 platelet endothelial cell adhesion molecule 1 (CD31), VE-cadherin (CD144), and CD34 expression were unchanged on day 1, but slightly rose on day 2. However these increased was non-statistically significant. The expression CD29, which represents mesenchymal stem cells, was stable on day 1 and 2.

After synthesis [35], EPCs were labeled by electroporation with the contrast agent Dex-DOTA-Gd^{3+}, whose structure is shown in Fig. 1A. Labeled EPCs showed bright fluorescence in the cytoplasm under the confocal scanning microscope, reflecting the presence of large amounts of contrast agent (Fig. 1B). Interestingly, magnified images of labeled cells (Fig. 1C) revealed that no further transport into the nucleus was observed 25 days after labeling.

It is well known that EPCs induce neovascularization by incorporating cells into formed vessels and releasing angiogenic factors in a paracrine manner [20,21]. We then examined the effect of Dex-DOTA-Gd^{3+} labeling on the expression of pro-angiogenic factors specific to EPCs such as VEGF, HGF, SDF-1, and IGF1. The expression of growth factors related to GAPDH in EPCs was not statistically different compared to Dex-DOTA-Gd^{3+}-labeled cells 2 days after electroporation ($P > 0.05$) (Fig. 1D).

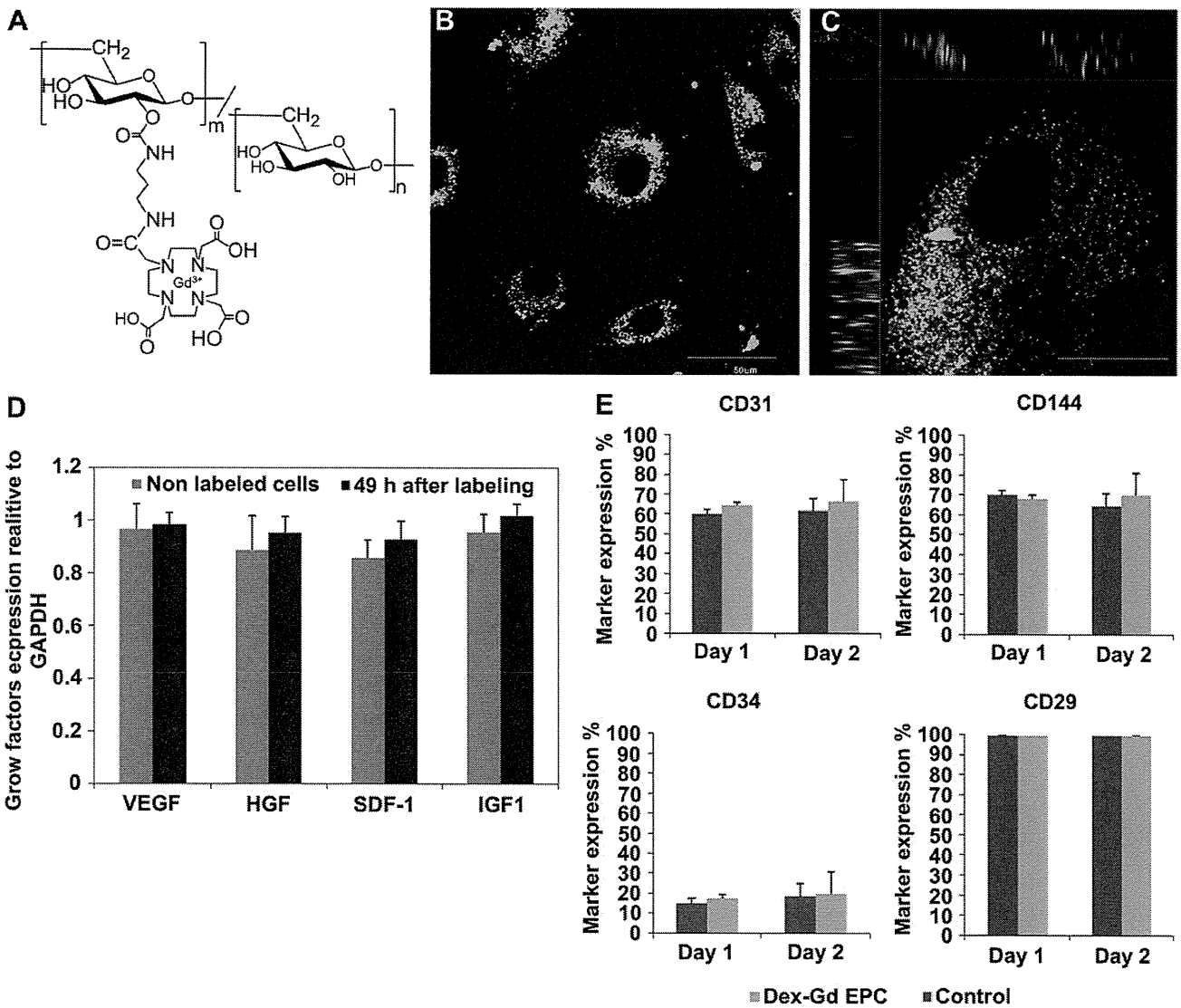

Fig. 1. Dextran-mono-N-succinimidyl 1,4,7,10-tetraazacyclododecane-1,4,7,10-tetraacetate-gadolinium^{3+} (Dex-DOTA-Gd^{3+}) as an magnetic resonance imaging (MRI) contrast agent. (A) Chemical structure of Dex-DOTA-$Gd.^{3+}$(B–C) Confocal microscopy of Dex-DOTA-Gd^{3+}-labeled endothelial progenitor cells (EPCs) after electroporation. Scale bar = 50 μm (left) and 25 μm (right). (D) Cellular expression levels of pro-angiogenic growth factors such as vascular endothelial growth factor (VEGF), hepatocyte growth factor (HGF), stromal cell-derived factor-1 (SDF-1), and insulin-like growth factor-1 (IGF-1) in Dex-DOTA-Gd^{3+}-labeled EPCs 48 h after electroporation. The mean (±SD) values of cellular expression relative to glyceraldehyde-3-phosphate dehydrogenase (GAPDH) are shown; no statistically significant differences were identified between labeled and unlabeled EPCs ($n = 6$) *$P > 0.05$. (E) EPC membrane marker expression. Percentage of the marker expression by FACS was performed in 4 different markers: CD31, CD144, CD34, and CD29, at days 1 and 2 after Dex-DOTA-Gd^{3+} labeling by electroporation. No significant changes in expression markers were observed on both days, compared to unlabeled EPC (control). FACS analysis was performed in triplicate, with three different samples, for all markers. Bars represent the standard deviation between different samples. No statistically significant differences were identified between labeled and unlabeled EPCs.

3.2. Effect of Dex-DOTA-Gd^{3+} on ischemic limb healing

We evaluated whether Dex-DOTA-Gd^{3+} as a contrast agent has an adverse effect on the capacity of EPCs to promote angiogenesis and neovascularization of ischemic limbs. Subcutaneous blood flow perfusion was analyzed using an LDPI (Fig. 2A). The ischemic limb blood perfusion ratios in animals implanted with Dex-DOTA-Gd^{3+}-labeled EPCs showed that blood perfusion increased after 5 days (red to white color distribution, 54% increase at day 30, $P < 0.001$) compared with control rats, in which an increase in blood perfusion was barely detected (Fig. 2B). On the basis of the results of the blood perfusion analysis, conventional angiograms were obtained 35 days after Dex-DOTA-Gd^{3+}-labeled EPCs were implanted in ischemic limbs. Microangiography allowed the visualization of the arterial network of an ischemic limb after transplantation of Dex-DOTA-Gd^{3+}-labeled EPCs and showed an increase in the number of small arteries after excision of the femoral artery and vein (Fig. 2D) [38]. Most of them originated from the trunk of the iliac artery. This gathering feature of the arteries was not observed in the branching pattern of control ischemic arteries (Fig. 2C). Angiography confirmed that Dex-DOTA-Gd^{3+}-labeled EPCs are capable of promoting the formation of collateral vessels in ischemic limbs.

Supplementary video related to this article can be found at doi: 10.1016/j.biomaterials.2011.11.075.

3.3. EPC migration in ischemic and non-ischemic limbs

Having demonstrated that MRI of EPCs by means of Dex-DOTA-Gd^{3+} did not affect the ability of EPCs to regenerate injured tissues, we tested the hypothesis that the behavioral pattern of these cells in an ischemic limb should differ from that in a non-ischemic limb and also from the pattern exhibited by SPIO-labeled cells, by using a different group of F344 rats (male, 8 weeks old $n = 3$). Rats were implanted with 1×10^7 labeled cells to analyze the pattern of migration exhibited by Dex-DOTA-Gd^{3+}-labeled EPCs in non-ischemic and ischemic limb models, as well in SPIO-labeled EPCs in ischemic models. The position of the animals in the MRI machine is indicated in Fig. 4A and was considered more adequate to understand the fate and migration of labeled EPCs. T1-weighted images of the rats were acquired with 2D and 3D spin-echo sequences at a TR of 2000 ms, a TE of 12 ms, coronal slice thickness of 1 mm, average 2, and image acquisition matrix of 128×256. Dex-DOTA-Gd^{3+} labeled EPCs transplanted into the ischemic limb were visualized within 14 days after transplantation. Cells were observed in the adductor and quadriceps, and migration in the direction of the knee muscle was as indicated by arrows in Supplementary Fig. 2. Labeled cells were completely banished after 14 days. To elucidate the spatial location and biodistribution of transplanted labeled cells, the acquired MRIs were modeled by the

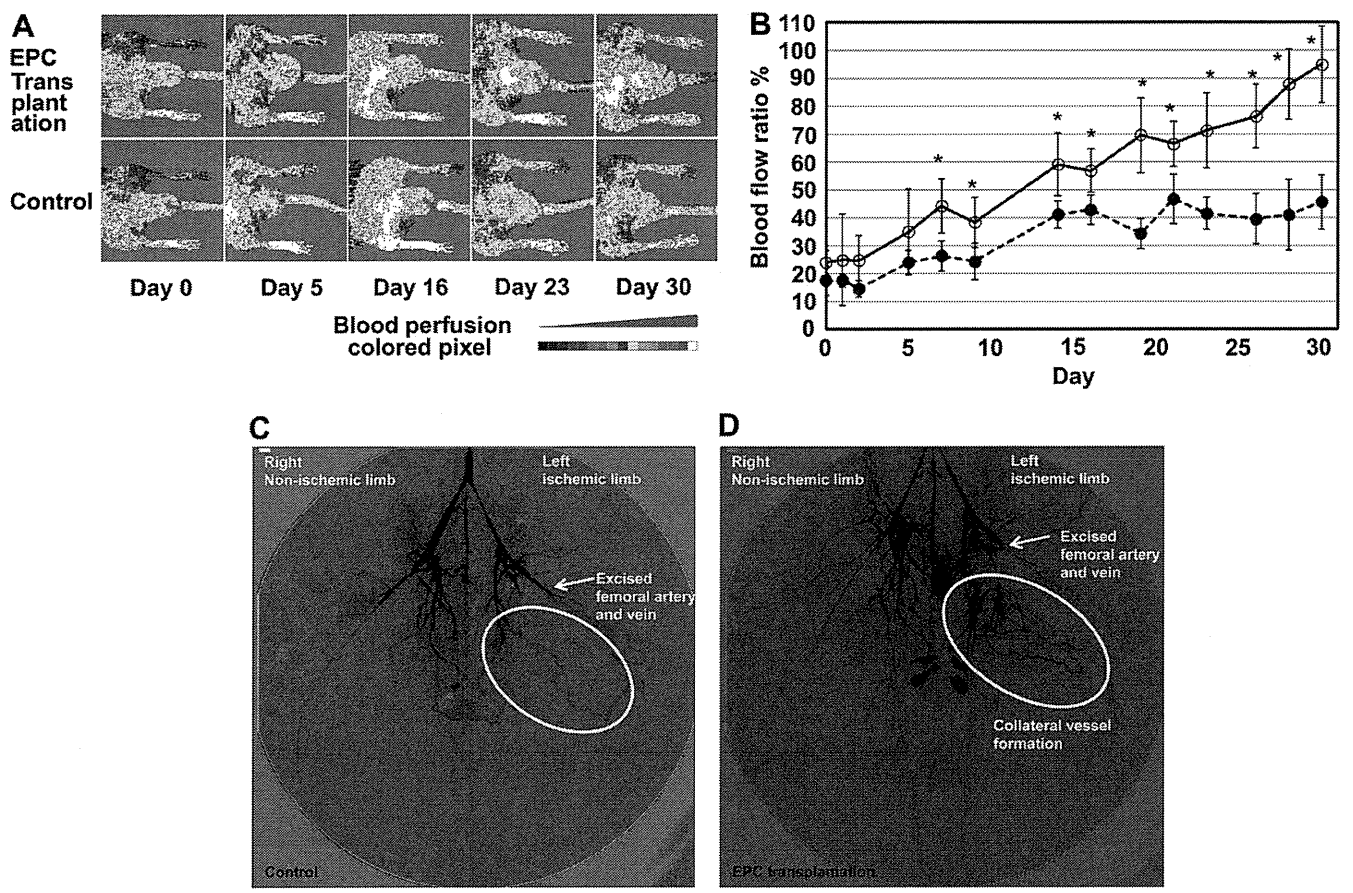

Fig. 2. Recovery of blood flow in ischemic limbs measured by using a Laser Doppler Perfusion Imager (LDPI). (A) A greater blood perfusion signal (red to white) was observed in the ischemic area where EPCs were transplanted. Blood flow ratio = cell flux/normal flux (B) Representative LDPI. Dex-DOTA-Gd^{3+} labeled EPCs transplanted into the ischemic limb (●, $n = 6$), control, non-labeled Dex-DOTA-Gd^{3+} cells (○, $n = 6$), values are mean (±SD) at each time point. $P > 0.05$ and $^*P < 0.001$ vs. control. (C) Representative angiograms of the non-ischemic limb model injected only with Bolheal® (control), and (D) rat ischemic limb model injected with 20×10^6 Dex-DOTA-Gd^{3+}-labeled EPCs in Bolheal® (EPC transplantation). Angiograms were performed after injection of the contrast agent (iodone) through a catheter inserted in the abdominal aorta ($n = 3$/group). Videos of the ischemic model after labeled cell implantation (video 1) and after 14 (video 2) are available as electronic supplementary data. (For interpretation of the references to colour in this figure legend, the reader is referred to the web version of this article.)

3D-Doctor software. The white and deep red colors represent the volume occupied by labeled cells (Fig. 3B and C, and Fig. 4). Consistent with the results shown in Supplementary Fig. 2, rendered MRIs obtained from the T1-weighted images (total 35) clearly exhibited the migration pattern of labeled EPCs in the ischemic limb. In contrast, MRIs of Dex-DOTA-Gd^{3+}-labeled EPCs transplanted into non-ischemic rat models showed the presence of transplanted cells in the muscle (Fig. 3C), but no significant movement was observed and cells gradually disappeared within 8 days post-transplantation. T1-weighted images of the non-ischemic limb confirmed the low capacity of cells to migrate.

Moreover, in a separate experiment, T2*-weighted images identified SPIO-labeled EPCs in the ischemic limbs (Supplementary Fig. 4). The area of MRI contrast appears to be extended in the limb. This could be partly due to the sensitivity of T2* imaging, which could induce disturbances in the magnetic field causing an amplification of the signal. However, SPIO-labeled cells seemed to remain static and detectable in the ischemic limb without apparent migration or loss of signal from the transplantation point after 21 days. The 3D rendered images better illustrate this behavior exhibited by SPIO-labeled cells (Fig. 4A).

One of the features of the 3D-Doctor software is that it enables the measurement of the volume occupied by the implanted labeled cells in the tissue. The volume of cells in the limb calculated with this software is shown in Figs. 3D and 4B. In all models, the volume of labeled implanted cells was around 500 mm^3. In the ischemic model, the volume of Dex-DOTA-Gd^{3+}-labeled EPCs increased while the cells were migrating, reaching a maximum value (2706 mm^3) at day 6 followed by a decrease due to the reduction of the signal of the contrast agent until day 16. In the non-ischemic model, on the other hand, the volume of the Dex-DOTA-Gd^{3+}-labeled EPCs barely increased on day 2 and rapidly diminished on day 8. This result is in disagreement with that obtained with SPIO-labeled EPCs, in which the volumes were not statistically different from day 1 until day 21 post-transplantation ($P > 0.05$).

3.4. Gadolinium clearance from the body

We first quantified the total amount of Gd in the transplanted labeled EPCs in the ischemic and non-ischemic models by ICP mass. After electroporation, we found that 1 EPC contained 0.83 pg of Gd for a total of 7.78 ± 0.73 μg Gd/rat transplanted in the limb (1.65×10^{-4} mmol/kg body weight [BW]). This dose was significantly lower (1814 times) than the average contrast material dosage used for human patients (0.3 mmol/kg BW = 18 mmol) [39].

Urine and feces were separately collected every 48 h from the metabolic cages in which ischemic and non-ischemic rat models were placed. After treatment with nitric acid, the quantity of Gd was measured by ICP mass. The percentage of Gd excreted from the rats in correlation to the total dose applied is shown in Fig. 5. Two different clearance profiles were observed in the samples. The total amount of Gd cleared from the non-ischemic rat models was 74% (5.73 μg) compared to 43% (3.4 μg) cleared in the ischemic model (Fig. 5). In both cases, Gd was gradually cleared via urine and feces until day 14, and the Gd clearance was suspended until day 20. Although the percentages of Gd excreted from the 2 rat models were not statistically different until day 6, significant differences in Gd clearance were revealed after day 8. Rat ischemic models cleared approximately 32% of the total Gd applied via the urine (2.49 μg), in contrast to non-ischemic rat models, in which 47% of the total Gd dose (3.67 μg) were cleared via urine. Similar results were obtained with regard to the Gd clearance via feces, in which the non-ischemic models cleared an additional 27% (2.06 μg) in comparison to the ischemic models (12%, 0.93 μg).

To further investigate whether the remaining Gd could be accumulated in different target organs, liver, lungs, and kidneys of the rat models were excised and treated with nitric acid to quantify the Gd using ICP mass (Supplementary Table 2). The results showed that Gd did not accumulate in the lungs of any of the rat models. However, a small amount of Gd was found in kidneys and livers from both rat models. The cumulative dose percentage of Gd in the kidneys of ischemic models was $7.4 \times 10^{-4} \pm 2.9 \times 10^{-4}$% (60.5 pg) and $9.1 \times 10^{-4} \pm 2.1 \times 10^{-4}$% (66.2 pg) in non-ischemic rats. The percentage of Gd in the livers was $8.9 \times 10^{-4} \pm 2.1 \times 10^{-4}$% (72.9 pg) and $9.9 \times 10^{-4} \pm 2.1 \times 10^{-4}$% (72.1 pg) for the ischemic and non-ischemic models, respectively.

3.5. Histological assessment of cell engraftment

In all animals implanted with SPIO, Berlin blue-positive cells were detected at the injection site in tissue sections (Fig. 6). To identify the iron-containing cells, sections adjacent to those exhibiting Berlin blue-positive cells from all rats killed at day 21 were tested for a macrophage-specific antigen (CD68 or macrosialin) by immunocytochemistry, which revealed several CD68-positive cells, with a staining pattern similar to that seen with Berlin blue-positive cells (Fig. 6A and B).

Moreover, sections corresponding to the Berlin blue-positive areas were tested for the presence of a specific EPC marker (vWF) and a negative marker (α-SMA).

Staining for vWF exposed many positive areas (brown color in Fig. 6C) in the sections derived from animals sacrificed at 21 days, and a similar pattern was obtained with α-SMA (brown color in Fig. 6D), which likely shows that EPCs already differentiated into the endothelial phenotype. This pattern, however, differed from that observed with Berlin blue. These results confirm the discordance between the MRI signal and the SPIO-labeled EPCs.

4. Discussion

The present findings revealed important characteristics of Dex-DOTA-Gd^{3+} as MRI contrast agent for stem cell therapy by identifying features of angiogenesis of ischemic tissues after transplantation of labeled EPCs that could have significant clinical and research implications. First, the reliability of Dex-DOTA-Gd^{3+} for the detection and tracking of living labeled EPCs by MRI for long periods was demonstrated. In addition, the clearance of free contrast agent, which was likely released from dead cells, via urine and feces was shown. Second, Dex-DOTA-Gd^{3+} can provide fundamental information on the migration phenomena likely caused by chemoattraction or paracrine effects to ensure proper incorporation at the site of revascularization of ischemic tissues. In addition, we examined the ability of SPIO as an MRI contrast agent for the tracking of labeled EPCs. A persistent MRI signal from the ischemic limbs after transplantation of SPIO-labeled EPCs might be the result of phagocytosis of iron nanoparticles by resident macrophages. Our findings showed the limitations of SPIO labeling methods in preclinical and clinical trials of stem cell therapy.

Preclinical studies have indicated that ex vivo EPC transplantation could be used to promote neovascularization of ischemic tissues by showing the augmentation of naturally impaired neovascularization in an animal model of induced ischemic limb [40,16]. Asahara et al. [15], reported that intravenously transfused EPCs contribute to neovascularization of ischemic tissues in an adult experimental animal. In a different study, BM-derived EPCs were shown to home and incorporate into the sites of vasculogenesis [1,37].

In a recent publication from our group [35], we described the synthesis and properties of Dex-DOTA-Gd^{3+} as an MRI contrast

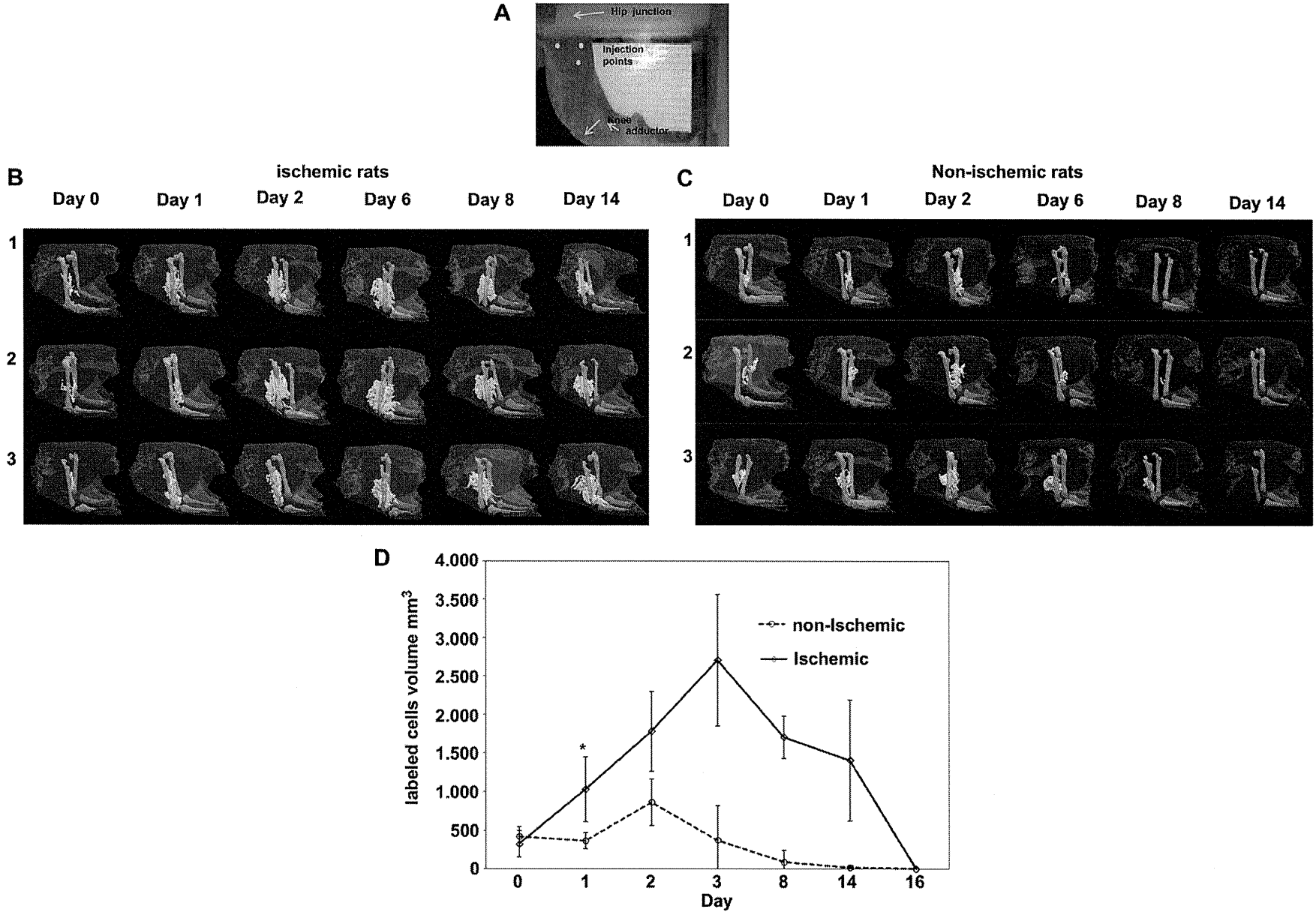

Fig. 3. Three-dimensional reconstructed MRIs of Dex-DOTA-Gd^{3+} labeled EPCs after intramuscular injection in ischemic limb rat models. (A) Rat position in the MRI indicating the injection points in the limb. (B) MRIs of the labeled EPC migration pattern in the ischemic limb in a rat ischemic limb model (F344, male, 8 weeks old, total 3 rats) in the inguinal region where the femoral artery and vein were excised. (C) Dex-DOTA-Gd^{3+}labeled EPC in non-ischemic models (total 3 rats). (D) Volume occupied by the implanted labeled cells in the tissue, as calculated using 3D-Doctor. Values represent mean (±SD) at each time point ($n = 3$/group). No statistically significant differences were detected between the ischemic and non-ischemic models after labeled cell transplantation at day 0, $^*P > 0.05$, while statistically significant differences were noted from days 1–14, $^*P < 0.001$. Overall, the different pattern of migration in the ischemic and non-ischemic models was due to the absence of released chemokines, which are known to mobilize EPCs, in response to vascular injury.

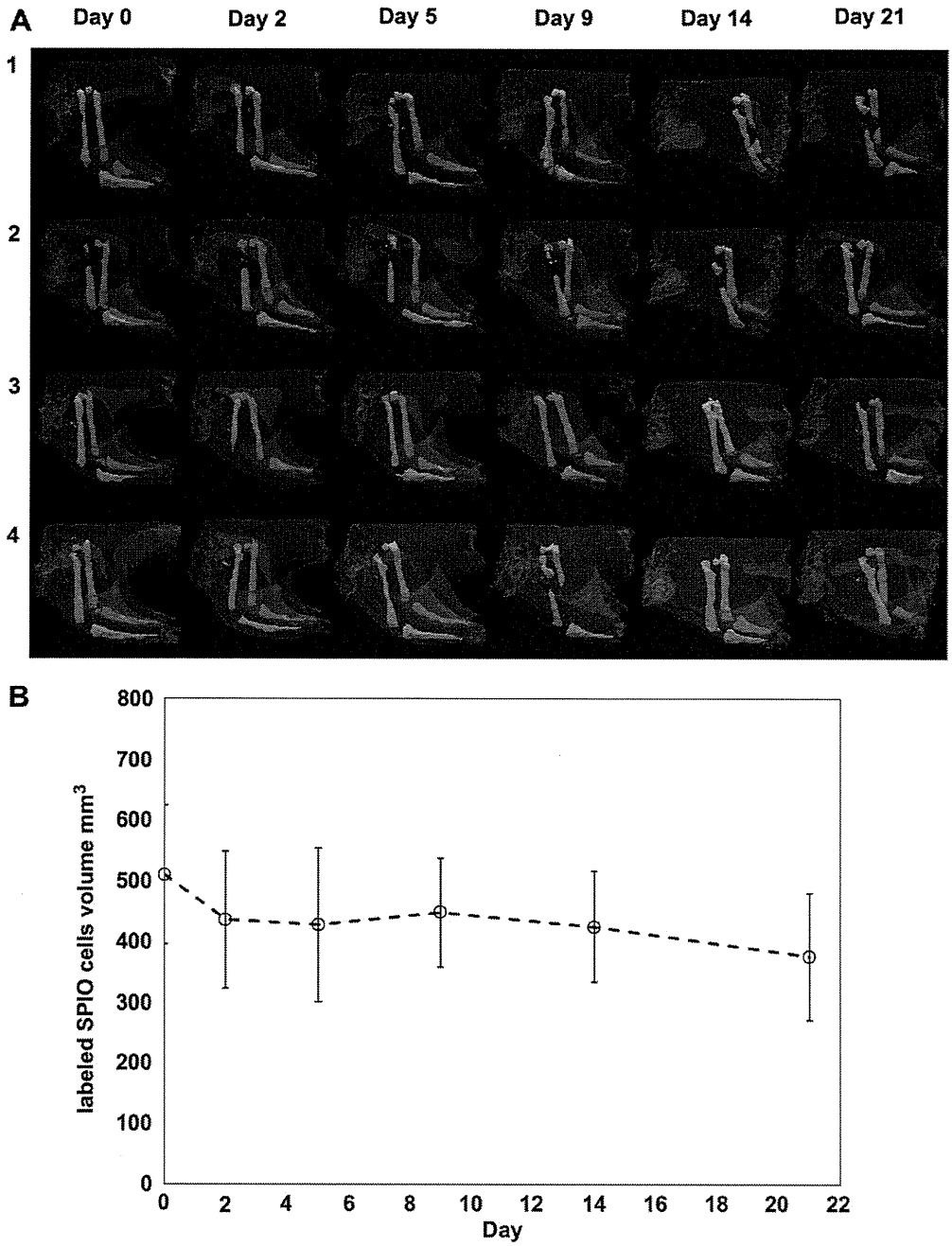

Fig. 4. Three-dimensional reconstructed (MRIs) of SPIO-labeled EPCs after intramuscular injection in rat ischemic limb models. (A) MRIs of SPIO-labeled EPCs in ischemic models (total 4 rats). (B) Volume occupied by the implanted labeled cells in the tissue calculated using 3D-Doctor. Values represent mean (±SD) at each time point ($n = 4$). No statistically significant differences were detected between day 0 and day 21 after labeled cell implantation. $P > 0.05$. Note the lack of migration in SPIO signal and the unviable volume in the ischemic model.

agent that satisfied certain conditions such as the provision of desired MRI contrast properties, ex vivo cell labeling before transplantation, highly sensitive and stable intracellular labeling (Fig. 1B and C), biocompatibility without affecting cell viability, proliferation or healing capacity by enhancing capillary formation, and the maintenance of consistently detectable signals for long periods of time. We also demonstrated that Dex-DOTA-Gd^{3+} was not taken up by resident macrophages and we double stain the Dex-DOTA-Gd^{3+} labeled EPC by Qtracker® 655. EPCs were localized in the neovascular zones of the ischemic limb ensuring that MRI signals correspond to signals generated by the labeled cells. In the present study, we assessed whether Dex-DOTA-Gd^{3+} has any adverse effects on the capacity of EPCs to release grow factors and promote angiogenesis and vasculogenesis in a rat ischemic limb model. The Dex-DOTA-Gd^{3+} labeled EPC were found that this labeling process (electroporation) barely affected the cell's biological properties. After, labeling, EPC continue to divide and proliferate as non-labeled cells. The expression of EPC membrane proteins was not statistically modified by the labeling (Fig. 1E). In particular, the expression of two adherence proteins, PECAM-1 and VE-cadherin

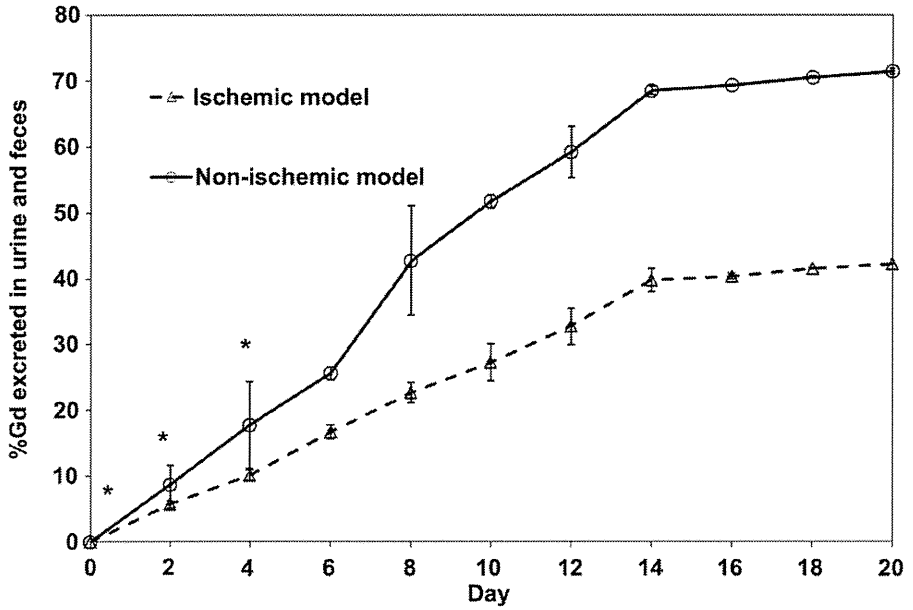

Fig. 5. Clearance of gadolinium (Gd) from the ischemic and non-ischemic models. Total percentage of Gd cleared from urine and feces. EPCs contained 0.83 pg of Gd of a total of 7.8 ± 0.73 μg Gd/rat transplanted in the limb (1.65×10^{-4} mmol/kg body weight). Urine and feces samples were treated with nitric acid before measurement by inductively coupled plasma atomic emission spectroscopy (ICP-AES). Samples were measured in duplicate. Values are mean (±SD) at each time point ($n = 3$). Note: error bars may be smaller than the symbols. No statistically significant differences were detected between day 0 and day 4 after labeled cell implantation; *$P > 0.05$. The difference was statistically significant from day 6 to day 20, $P < 0.01$.

that are involved in vascular integrity. The VE-cadherin is fundamental for vascular tube formation and participates in cell survival signaling by interaction with beta catenin, VEGF-R2, and PI3 kinase complexes [23]. Flow cytometry showed that the EPC phenotype remained stable after Dex-DOTA-Gd^{3+} labeling by electroporation.

Consistent with our previous study, the results presented herein demonstrated that Dex-DOTA-Gd^{3+} as an MRI contrast agent did not influence the capacity of blood perfusion restoration (Fig. 2A and B), collateral vessel formation (Fig. 2D), and expression of growth factors, which in turn support the survival and function of

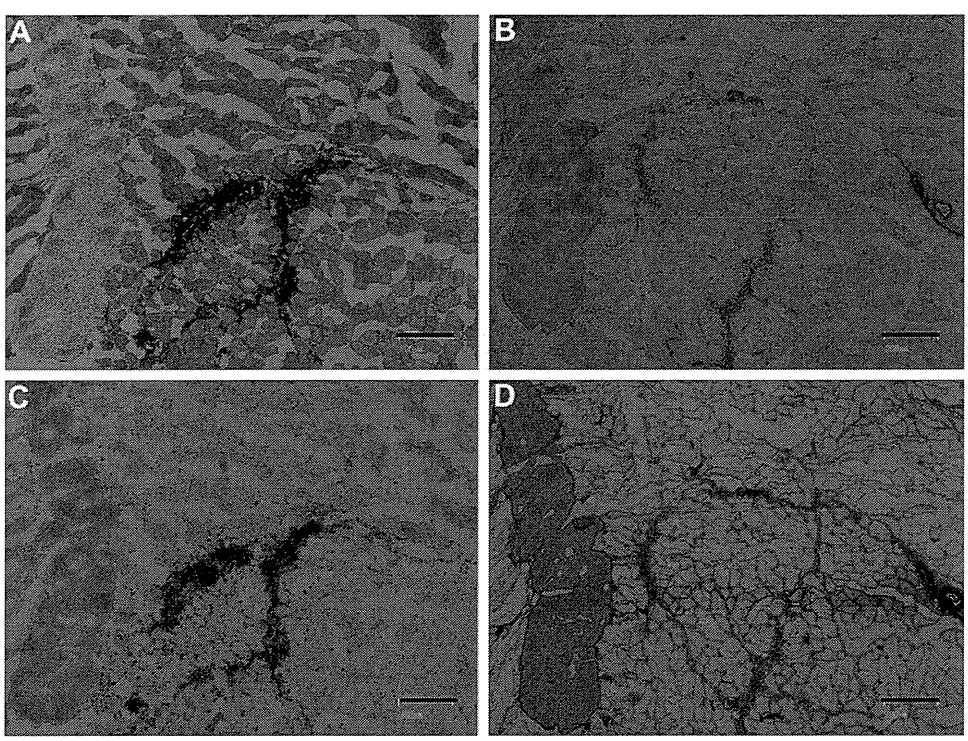

Fig. 6. Representative histology of rat ischemic tissue harvested 21 days after transplantation of SPIO-labeled EPCs. (A) Berlin blue staining shows the presence of large groups of iron-containing cells in an animal implanted with EPCs. (B) CD68 immunostaining showing a large number of positive cells (macrophages) with a pattern similar to that of Berlin blue-positive cells. (C) von Willebrand factor (vWF) and (D) alpha smooth muscle actin (α-SMA)-positive cells in a rat implanted with SPIO-labeled EPCs.

tissue resident cells, and consequently, enhance the vasculogenesis process and regeneration of ischemic limbs [19].

MRI as a high-resolution technique for tracking EPCs in vivo can provide important insights on the different phenomena associated with angiogenesis of ischemic limb models [15–17,22]. In vivo MRIs (Fig. 3B and Supplementary Fig. 2) indicated that Dex-DOTA-Gd^{3+}-labeled EPCs are perfectly detectable and the fate of the cells can be followed within 14 days after transplantation. When acquiring T1-weighted MRIs, Dex-DOTA-Gd^{3+}-labeled EPCs transplanted into an ischemic limb model exhibited a pattern of migration in which cells moved along the adductor in the direction of the knee mobilized by chemoattraction to the foci of vasculogenesis, thus restoring blood perfusion. This particular migration pattern was observed in all of the studied animal models. In contrast, MRIs of Dex-DOTA-Gd^{3+}-labeled EPCs transplanted into a non-ischemic limb model showed a different pattern. Cells were not mobilized from the injection point and remained in that location until they disappeared within 8 days post-transplantation. This is probably due to the absence of chemokines in the non-ischemic model. Dex-DOTA-Gd^{3+}-labeled EPCs could no longer remain alive in the limb, and the contrast agent in the cells was cleared from the body.

In ischemic models implanted with SPIO-labeled EPCs, the anatomic location of labeled cells at the injection point can be efficiently tracked. Despite the fact that EPCs transplanted into ischemic tissues are expected to migrate and be incorporated into vessel structures [21], SPIO-labeled cells did not show migration, and the fate of EPCs could not be monitored in the long term. Remarkably, no differences in the MRI scans could be observed from day 1 to day 21. Further immunohistological analysis at day 21 after cell transplantation identified the SPIO-containing cells as tissue macrophages. The uptake of SPIO by these infiltrated cells led to the persistence of iron at the injection site, which generated the signal on the MRIs. Previous studies demonstrated that transplantation of iron-labeled cells enabled tracking of the cells over time [23,24,41]. However, several studies have found that iron nanoparticles are not consistent markers to track the fate and survival of transplanted labeled stem cells.

Clearance of Gd from the rat models via urine and feces demonstrated that the living Dex-DOTA-Gd^{3+}-labeled EPCs can be tracked over long periods of time, while the contrast agent contained in dead cells is released and cleared from the body. In the ischemic models, 43% of the total Gd incorporated in the labeled cells was gradually cleared via urine and feces within 14 days post-transplantation (Fig. 5), ensuring that the living Dex-DOTA-Gd^{3+}-labeled cells were the only cells tracked by MRI. In non-ischemic models, 74% of the total Gd was progressively excreted, indicating that labeled cells slowly died, thereby releasing the excess label. However, living labeled cells where tracked for about 8 days, were completely banished within 14 days (Fig. 3C, only in model 2), and did not migrate in the ischemic limb. The amount of Gd excreted in the non-ischemic models was higher (31%) than in the ischemic models, suggesting that the Gd clearance profiles are different in the 2 models. These results confirm the reliability of Dex-DOTA-Gd^{3+} as MRI contrast agent for tracking living cells.

The amounts of Gd cleared via urine and feces were separately measured by ICP mass. However, we combined the amounts of Gd from urine and feces (Fig. 5) because despite the use of metabolic cages to separately collect feces and urine, absorption of urine by feces could not be avoided in some cases. Moreover, a significant quantity of urine was attached to and dried in the cage walls and supporting rat meshes. Because we expected all of the Gd incorporated in labeled cells to be released in the non-ischemic models, and because the amount of Gd from kidneys and livers was extremely low in comparison with the total dosage, we assumed that the loss of Gd in the cages amounted to approximately 26.5% of the total (2.1 μg). However, we believe that the loss of Gd in the ischemic models was lower. Despite the limitations in collecting the excrements in animal models, we believe that this method can be applied to clinical trials due to the better control of collecting the excrements, which would allow a more accurate estimation of the total Gd cleared from the body.

Gd ions released from contrast agents have been suspected to play a role in nephrogenic systemic fibrosis (NSF) in patients with primary renal disease [39]. Although Gd ions strongly bind DOTA and form stable chelates [42], the possible presence of free Gd ions cannot be ruled out. To avoid this situation, we used a Gd/DOTA ratio in Dex-DOTA-Gd^{3+} of 0.78; the remaining empty DOTA in the polymer was 0.22 (polymer unit). Consequently, Gd released from the chelates can be captured by the Dex-DOTA-Gd^{3+} complex because of the available DOTA groups near the free Gd ions.

The common clinical dosage of MRI contrast agents is 1800 times higher than the dosage used for Dex-DOTA-Gd^{3+}-labeled stem cells. In addition, the incorporation of DOTA-Gd^{3+} into dextran probably increased the relaxation time due to a steric limitation on the rotational movement of the polymer, which increased the rotational correlation coefficient [42]. Therefore, the quantity of contrast agent necessary to enhance the imaging results is considerably lower than that used in Gd complex contrast agents such as DOTA-Gd^{3+} and Magnevist® which exhibit a relatively slow relaxation time in comparison with Dex-DOTA-Gd.$^{3+}$ [35].

BM-derived Dex-DOTA-Gd^{3+}-labeled EPCs that survived in the ischemic limbs were incorporated into the sites of neovascularization and promoted the collateral vessels formation. Dex-DOTA-Gd^{3+} did not probably affect the mobilization, chemoattraction, or adhesion of EPCs with regard to the regeneration of ischemic tissue.

5. Conclusion

Our results demonstrated the reliability of Dex-DOTA-Gd^{3+} as MRI contrast agent for labeling of BM-derived EPCs by electroporation and tracking of labeled stem cells in ischemic limbs over time. MRI was capable of distinguishing living cells from dead cells because the Dex-DOTA-Gd^{3+} freed from dead cells was rapidly cleared from the body. In contrast, although SPIO was useful for monitoring the anatomic location of labeled cells, it did not provide consistent information on long-term cell viability. The present analysis of MRIs provides evidence of how cell migration occurs along the muscle to the ischemic site, showing a different pattern of migration than that observed in non-ischemic limbs. These achievements in the in vivo assessment of cell migration are a crucial contribution to the advancement of human stem cell-based therapies.

Author contributions

C.A.A., T.Y., and Y.T conceived and designed all studies. A.F.H. and C.A.A. edited the MRI scans. H.I. and T.O. contributed with the implementation of the rat ischemic limb model and MRI studies along with C.A.A. Paper was wrote by C.A.A. All experiments were performed by C.A.A.

Acknowledgments

This work was supported by grants-in-aid from the Ministry of Health, Labour, and Welfare of Japan (Health and Labour Sciences Research Grants, Research on Nanotechnical Medicine). This work was supported by a Research Grant for Cardiovascular Diseases

(18A-2) from the Ministry of Health, Labour, and Welfare of Japan, and Japan Association for the Advancement of Medical Equipment. The authors thank Jun-ichiro Enmi, Teramoto Noboru, Hajime Fukuda, and Akihide Yamamoto for their cooperation during this project.

Appendix. Supplementary material

Supplementary material associated with this article can be found, in the online version, at doi:10.1016/j.biomaterials.2011.11.075.

References

[1] Rafii S, Lyden D. Therapeutic stem and progenitor cell transplantation for organ vascularization and regeneration. Nat Med 2003;9:702–12.
[2] Kondo K, Shintani S, Shibata R, Murakami H, Murakami R, Imaizumi M, et al. Implantation of adipose-derived regenerative cell enhances ischemia induced angiogenesis. Arterioscler Thromb Vasc Biol 2009;29:61–6.
[3] Murohara T. Autologous adipose tissue as a new source of progenitor cells for therapeutic angiogenesis. J Cardiol 2009;53:155–63.
[4] Shintani S, Murohara T, Ikeda H, Ueno T, Sasaki K, Duan J, et al. Augmentation of postnatal neovascularization with autologous bone marrow transplantation. Circulation 2001;103:897–903.
[5] Hida N, Nishiyama N, Miyoshi S, Kira S, Segawa K, Uyama T, et al. Novel cardiac precursor-like cells from human menstrual blood-derived mesenchymal cells. Stem Cells 2008;26:1695–704.
[6] Iba O, Matsubara H, Nozawa Y, Fujiyama S, Amano K, Mori Y, et al. Angiogenesis by implantation of peripheral blood mononuclear cells and platelets into ischemic limbs. Circulation 2002;106:2019–25.
[7] Kocher AA, Schuster MD, Szabiolcs MJ, Takuma S, Burkhoff D, Wang J, et al. Neovascularization of ischemic myocardium by human bone marrow derived angioblast prevents cardiomyocyte apoptosis, reduces remodeling and improves cardiac function. Nat Med 2001;7:430–6.
[8] Leobon B, Roncalli J, Joffre C, Mazo M, Boisson M, Barreau C, et al. Adipose-derived cardiomyogenic cells: in vitro expantion and functional improvement in a mouse model of myocardial infarction. Cardiovasc Res 2009;83:757–67.
[9] Rafii S, Meeus S, Dias S, Hattori K, Heissig B, Shemelkov S, et al. Contribution of morrow-derived progenitors to vascular and cardiac regeneration. Cell Devl Biol 2002;13:61–7.
[10] Risau W. Mechanism of angiogenesis. Nature 1997;386:671–4.
[11] Folkman J, D'Amore PA. Blood vessel formation: what is its molecular basis? Cell 1996;87:1153–5.
[12] Asahara T, Masuda H, Takahashi T, Kalka C, Pastore C, Silver M, et al. Bone marrow origin of endothelial progenitor cells responsible for postnatal vasculogenesis in physiological and pathological neovascularization. Circ Res 1999;85:221–8.
[13] Shi Q, Rafii S, Wu MH, Wijelath ES, Cong Y, Ishida A, et al. Evidence for circulating bone marrow-derived endothelial cells. Blood 1998;92:362–7.
[14] Kalka C, Masuda H, Takahashi T, Gordon R, Tepper O, Gravereaux E, et al. Vascular endothelial growth factor$_{165}$ gene transfer augments circulating endothelial progenitor cells in human subjects. Circ Res 2000;86:1198–202.
[15] Asahara T, Murohara T, Sullivan A, Silver M, Zee RVD, Li T, et al. Isolation of putative progenitor endothelial cells for angiogenesis. Science 1997;274:964–7.
[16] Iwaguro H, Yamaguchi JI, Kalka C, Murasawa S, Masuda H, Hayashi SI, et al. Endothelial progenitor cell vascular endothelial growth factor gene transfer for vascular regeneration. Circulation 2002;105:732–8.
[17] Lyden D, Hattori K, Dias S, Costa C, Blaikie P, Butros L, et al. Impaired recruitment of bone-marrow-derived endothelial and hematopoietic precursor cells blocks tumor angiogenesis and growth. Nat Med 2001;7:1194–200.
[18] Kalka C, Masuda H, Takahashi T, Kalka-Moll WM, Silver M, Kearney M, et al. Transplantation of ex vivo explanted endothelial progenitor cells for therapeutic neovascularization. Proc Natl Acad Sci USA 2000;28:3422–7.
[19] Urbich C, Aicher A, Heeschen C, Dernbach E, Hofmann WK, Zeiher AM, et al. Soluble factors released by endothelial cells and cardiac resident progenitor cells. J Mol Cell Cardiol 2005;39:733–42.
[20] Urbich C, Dimmeler S. Endothelial progenitor cells characterization and role in vascular biology. Circ Res 2004;95:343–53.
[21] Urbich C, Heesechen C, Aicher A, Dernbach E, Zeiher AM, Dimmeler S. Relevance of monocytic features for neovascularization capacity of circulating endothelial progenitor cells. Circulation 2003;108:2511–6.
[22] Lewin M, Carlesso N, Tung CH, Tang TX, Cory D, Scadden DT, et al. Tat peptide-derivatized magnetic nanoparticles allow in vivo tracking and recovery of progenitor cells. Nat Biotechnol 2000;18:410–4.
[23] Wilhelm C, Bal L, Smirnov V, Galy-Fauroux I, Clement O, Gazeau F, et al. Magnetic control of vascular network formation with magnetically labeled endothelial progenitor cells. Biomaterials 2007;28:3797–806.
[24] Bulte JWM, Douglas T, Witwer B, Zhang SC, Strable E, Lewis BK, et al. Magnetodendrimers allow endosomal magnetic labeling and in vivo tracking of stem cells. Nat Biotechnol 2001;19:1141–7.
[25] Guzman R, Uchida N, Bliss TM, He D, Christopherson KK, Stellwagen D, et al. Long term monitoring of transplanted human neural stem cells in developmental and pathological contexts with MRI. Proc Natl Acad Sci USA 2007;104:10211–6.
[26] Hoehn M, Küstermann E, Blunk J, Wiedermann D, Trapp T, Wecker S, et al. Monitoring of implanted stem cell migration in vivo: a highly resolved in vivo magnetic resonance imaging investigation of experimental stroke in rat. Proc Natl Acad Sci USA 2002;25:16267–72.
[27] Amsalem Y, Mardor Y, Feinberg MS, Landa N, Miller L, Daniels D, et al. Iron-oxide labeling and outcome of transplanted mesenchymal stem cells in the infarcted myocardium. Circulation 2007;116:I.38–45.
[28] Terrovitis J, Stuber M, Youssef A, Preece S, Leppo M, Kizana E, et al. Magnetic resonance imaging overestimates ferumoxide-labeled stem cell survival after transplantation in the heart. Circulation 2008;117:1555–62.
[29] Li Z, Suzuki Y, Huang M, Cao F, Xie X, Connolly AJ, et al. Comparison of reporter gene and iron particle labeling for tracking fate of human embryonic stem cells and differentiated endothelial cells in living subjects. Stem Cells 2008;26:864–73.
[30] Winter EM, Hogers B, Van der Graaf LM, Gittenberger-de Groot AC, Poelmann R, Van der Weerd L. Cell tracking using iron oxide fails to distinguish dead from living transplanted cells in the infracted heart. Magn Reson Med 2010;63:817–21.
[31] Tachibana Y, Enmi JI, Mahara A, Iida H, Yamaoka T. Design and characterization of a polymeric MRI contrast agent based on PVA for in vivo living-cell tracking. Contrast Media Mol Imaging 2010;5:309–17.
[32] Yamaoka T, Tabata Y, Ikada Y. The fate of water-soluble polymers administered through different routes. J Pharm Sci 1995;84:349–54.
[33] Yamaoka T, Tabata Y, Ikada Y. Blood clearance and organ distribution of intravenously administered polystyrene microspheres of different sizes. J Bioact Compat Polym 1993;8:220–35.
[34] Yamaoka T, Tabata Y, Ikada Y. Body distribution profile of polysaccharides after intravenous administration. Drug Deliv 1993;1:75–82.
[35] Agudelo CA, Tachibana Y, Noboru T, Iida H, Yamaoka Y. Long-term in vivo magnetic resonance imaging tracking of endothelial progenitor cells transplanted in rat ischemic limbs and their angiogenic potential. Tissue Eng 2011;15-16:2079–89.
[36] Takahashi T, Kalka C, Masuda H, Chen D, Silver M, Kearney M, et al. Ischemia- and cytokine-induced mobilization of bone marrow- derived endothelial progenitor cells for neovascularization. Nat Med 1999;5:434–8.
[37] Takeshita S, Takaaki I, Mori H, Tanaka E, Eto K, Miyazawa Y, et al. Use of synchrotron radiation microangiography to assess development of small collateral arteries in a rat model of hindlimb ischemia. Circulation 1997;95:805–8.
[38] Ikenaga S, Hamano K, Nishida M, Kobayashi T, Li T, Kobayashi S, et al. Autologous bone marrow implantation induced angiogenesis and improved deteriorated exercise capacity in a rat ischemic hindlimb model. J Surg Res 2001;96:277–83.
[39] Marckmann P, Skov L, Rossen K, Dupont A, Damholt MB, Heaf JG, et al. Nephrogenic systemic fibrosis: suspected causative role of gadodiamide used for contrast-enhanced magnetic resonance imaging. J Am Soc Nephrol 2006;17:2359–62.
[40] Nissen NN, Polverini PJ, Koch AE, Volin MV, Gamelli RL, DiPietro LA. Vascular endothelial growth factor mediates angiogenic activity during the proliferative phase of wound healing. Am J Pathol 1998;152:1445–52.
[41] Daldrun-Link HE, Rudelius M, Metz S, Brauer R, Debus G, Corot C, et al. Migration of iron oxide labeled human hematopoietic progenitor cells in a mouse model: in vivo monitoring with 1.5-T MR imaging equipement. Radiol 2005;234:197–205.
[42] Caravan P, Ellison JJ, McMurry TJ, Lauffer RB. Gadolinium (III) chelates as MRI contrast agent: structure, dynamics, and applications. Chem Rev 1999;99:2293–352.

Ann Nucl Med (2012) 26:214–221
DOI 10.1007/s12149-011-0561-4

ORIGINAL ARTICLE

Monte Carlo simulation of scintillation photons for the design of a high-resolution SPECT detector dedicated to human brain

Yoshiyuki Hirano · Tsutomu Zeniya · Hidehiro Iida

Received: 15 June 2011 / Accepted: 23 November 2011 / Published online: 13 December 2011

Abstract
Objective In a typical single photon emission computed tomography (SPECT) system, intrinsic spatial resolution depends on the accuracy of the identification of an interacting point, which is dominated by propagation of the scintillation photons in the detector block. This study was intended to establish a Monte Carlo simulation-based evaluation tool taking into account the propagation of scintillation photons to estimate the intrinsic spatial and energy resolutions of the position-sensitive scintillator block in a SPECT detector.
Methods We employed Geant4 Monte Carlo simulation library which incorporated the optical photon processes for two different designs of the position-sensitive scintillator blocks. The validation of the simulation code was performed for a monolithic NaI(Tl) scintillator (251 × 147 × 6.4 mm^3) coupled to 15 flat-panel type multi-anode photo multiplier tubes (PMT) (H8500: Hamamatsu) and results were compared with those obtained experimentally. The code was then applied to a $LaBr_3$(Ce) scintillator of 120 mm square with varied thicknesses for designing high-resolution detector.
Results The simulation resulted in 2.6 mm full width at half maximum (FWHM) of spatial resolution and 9.0% FWHM of energy resolution for the NaI(Tl)-based detector, which were in a good agreement of the experimental results, i.e., 2.7 mm and 10%, respectively. These findings suggest that Geant4 simulation including optical photon processes enables to predict the spatial and energy resolutions of a SPECT detector block accurately. The simulation also demonstrated that 2 mm spatial resolution can be obtained for a 6 mm thickness of the $LaBr_3$(Ce), which is a significant improvement in performance as compared to existing gamma camera system that employs the scintillation detector fitted with PMTs.
Conclusions The Monte Carlo simulation-based evaluation tool was established to estimate the intrinsic spatial and energy resolutions of SPECT detector with position sensitive PMTs. This simulation may be useful to provide an optimal design of a SPECT detector without physical experiments.

Keywords $LaBr_3$(Ce) · Monte Carlo simulation · Geant4 · SPECT · Scintillation photon

Introduction

Single photon emission computed tomography (SPECT) is capable of providing tomographic images of radiolabeled tracers in vivo. The equipment essentially consists of position-sensitive detectors fitted with several types of collimators, which rotate around the object to be imaged. In most SPECT detectors, the point of interaction between a gamma ray and a scintillation crystal is identified by Anger logic on a 2-dimensional domain. Interacting coordinates are calculated by a weighted mean of the deposition of scintillation photons. Spatial resolution depends on the accuracy of identification, which may be degraded as a result of the propagation of scintillation photons within the detector system.

A Monte Carlo simulation is a helpful tool in designing a new detector block. The simulation code is often useful when optimizing design parameters of the detector block,

Y. Hirano (✉) · T. Zeniya · H. Iida
Department of Bio-medical Imaging,
National Cerebral and Cardiovascular Center Research Institute,
5-7-1 Fujishiro-dai, Suita, Osaka 565-8565, Japan
e-mail: hirano@ri.ncvc.go.jp

e.g., the thickness and other geometric parameters of the scintillator as well as the scintillator material, without the need for physical experiments. In order to estimate intrinsic spatial resolution and energy resolution, it is essential to understand the process of transport of scintillation photons in the detector system, as well as the interaction of gamma rays with materials. Geant4 [1] makes it possible to simulate both these processes. Simulation studies on propagation of scintillation photons have been performed using Geant4 (or other code) [2–6]. However, it is difficult to reproduce the intrinsic spatial and energy resolutions accurately due to the many unknown factors (e.g., optical properties of materials and electrical noise) to simulate transporting scintillation photons. Resolutions essentially depend on the number of obtained scintillation photons. Geant4 does not include the optical properties of materials, such as absorption length, refraction index, and reflection. These data must be entered into Gean4 by users. The simulation accuracy is sensitive to these optical parameters. To our knowledge, a validation study on spatial and energy resolutions using Geant4 was performed only by Van Der Laan et al. [2] for a positron emission tomography (PET) instrument that employed a monolithic scintillators (LYSO(Ce): $20 \times 10 \times 10$ mm^3 and $20 \times 10 \times 20$ mm^3) and avalanche photodiodes (APD).

In this work, we intended to use Geant4 for two types of position-sensitive scintillation detector in a SPECT system. Both detectors consist of a monolithic scintillator and flat-panel type multi-anode PMTs (H8500: Hamamatsu). These are different from detectors used in previous study [2] regarding scintillator material, detector size and photo-sensors. With regard to photo-sensor, detection principle of PMT is absolutely different from that of APD. One detector has a larger field-of-view (FOV) and is fitted with a parallel beam collimator for imaging the whole human brain. The detector block consists of a NaI(Tl) scintillator ($251 \times 147 \times 6.4$ mm^3) and 15 PMTs. Its experimental physical performance was used to validate the simulation code, including the photon propagation processes. We then extended this simulation geometry to another detector block, which consists of a $LaBr_3$(Ce) scintillator [7, 8] coupled to 4 PMTs to achieve higher intrinsic spatial resolution. This detector has smaller FOV and may be fitted with a pinhole collimator for focused imaging of a limited area of the brain with higher spatial resolution of approximately 1 mm [9]. We also investigated effects of inclined incident angle of gamma rays into the detector in a pinhole configuration on spatial resolution of the detector system.

Materials and methods

Monte Carlo simulation

We employed the Monte Carlo simulation library Geant4 (version 9.2.p02) in this study. Geant4 enables us to simulate not only interaction of gamma rays with several materials but also transport of scintillation photons. In this simulation, we took into account the following electromagnetic processes: Compton scatter, photo-electric effect, Rayleigh scatter, multiple scatter, bremsstrahlung, and ionization. The first three processes involve gamma rays; the rest involve electrons. Optical photon processes in the propagation of scintillation photons were also included: absorption, Rayleigh scatter, reflection, and refraction.

Simulations were carried out for essentially two sets of detector configurations as follows. The two sets of detector configurations (large-FOV detector and small-FOV detector) were precisely reproduced as shown in Fig. 1. The simulation configurations included scintillator, reflector, optical window, optical grease, PMT window, and PMT cathodes. Gamma rays entered the detector vertically,

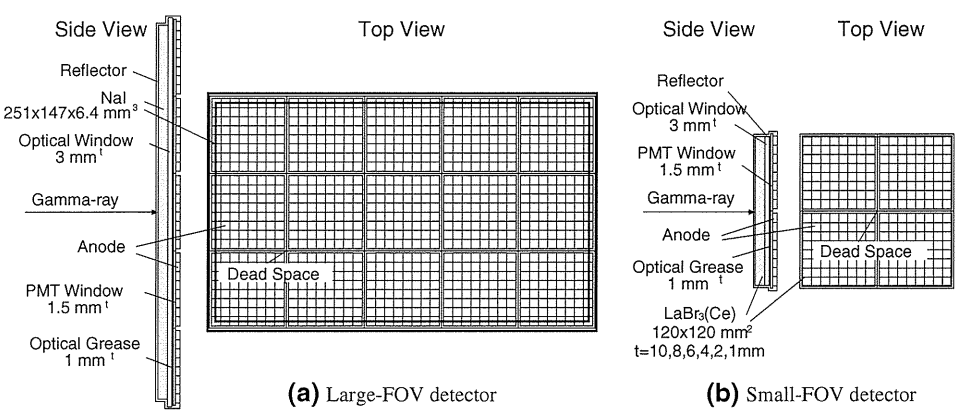

Fig. 1 Geometrical configurations of the large-FOV detector (**a**) and the small-FOV detector (**b**). In the simulation, we included the scintillator, reflector, optical window, optical grease, PMT window, and PMT anodes. The scintillator thickness of the small-FOV detector was varied (10, 8, 6, 4, 2, and 1 mm)

except for the simulation carried out for a pinhole configuration. When a gamma ray interacted with the scintillator and deposited its energy, scintillation photons were emitted isotropically. The emission spectra of NaI(Tl) and $LaBr_3$(Ce) are shown in Fig. 2a. The number of scintillation photons followed the Poisson distribution, and the mean was proportional to the energy deposition ($LaBr_3$(Ce): 63 photons/keV; NaI(Tl): 38 photons/keV). The scintillation photons propagated in the scintillator, optical window, optical grease and PMT window. At the reflector, the Lambert reflection was applied. The reflectance was 0.95 (white plastic). For a photon that was not reflected, propagation was terminated. At other boundaries between materials, the Fresnel reflection or Fresnel refraction was applied. When scintillation photon reached a cathode, the detection was determined by the quantum efficiency (Fig. 2a, gray line) and the collection efficiency (60%) of the H8500. The interacting point was reconstructed by Anger logic. An error of 17% was assigned to the anode gain. The error was estimated from anode uniformity map described in the specification. Transmittances of NaI(Tl) and borosilicate glass are shown in Fig. 2b. PMT cathodes and dead space surrounding the cathodes were assumed to be perfect absorbers. This simulation did not include absorptions by $LaBr_3$(Ce) and optical grease, because these transmittance data are not available. However, according to [10], the absorption for visible light is low. The thickness of optical grease was assumed as 1 mm. Refractive indices of, NaI(Tl), $LaBr_3$(Ce) and optical grease are 1.85, 1.9 and 1.465, respectively. With regard to borosilicate glass, the index was shown in Fig. 2c. These data were obtained from each specification.

Validation of the simulation code

To validate the Monte Carlo simulation, we compared spatial and energy resolutions obtained from the simulation with experimental values for the large-FOV detector. The experimental setup was as follows. The detector consisted of a monolithic NaI(Tl) scintillator (Saint-gobain) of 251 × 147 × 6.4 mm^3, fitted to 15 flat-panel type multi-anode PMTs (H8500: Hamamatsu) arranged in a 5 × 3 array. Each of the PMTs had 64 cathodes (8 × 8 array) that measured 5.8 mm square (6.08 mm pitch at center). The size of each PMT was 52 × 52 mm^2, and the PMT window was a 1.5 mm thickness of borosilicate glass that was transparent to visible lights. The NaI(Tl) scintillator was covered with a white diffuse reflector and an optical window of 3 mm thickness at the connection side of the PMTs. The optical window was also made of borosilicate glass. The NaI(Tl) scintillator was coupled to the PMTs by optical grease (BC630: Saint-gobain). Electric resistance arrays were connected to the anode outputs. The sum of the anode outputs and the positional coordinate (x, y) calculated by Anger logic were recorded in list mode. A specially designed collimator was placed in front of the detector block. The collimator was a 300 × 200 × 10 mm^3 block of lead with 170 holes of 1.5 mm diameter arranged in a 17 × 10 grid pattern with a grid interval of 15 mm. Small-tube sources (7 mm diameter) filled with Tc-99m solution were placed on 170 collimator holes, and position dependency of the energy spectra and point spread functions were measured. Energy and spatial resolutions were then evaluated.

In the simulation, spatial and energy resolutions were evaluated for the NaI(Tl)-based large-FOV detector by exposing 3000 gamma rays (141 keV) to the detector as a parallel beam with a circular distribution of 1.5 mm diameter at each of the hole positions. Interactions with the collimator were not included to reduce the computing time.

Application to the design of a new detector

Another series of simulations were carried out for the small-FOV detector to optimize the geometrical parameters. The scintillator was assumed to be $LaBr_3$(Ce) with a surface area of 120 × 120 mm^2. The scintillator was coupled to 4 PMTs (H8500) arranged in a 2 × 2 array. The

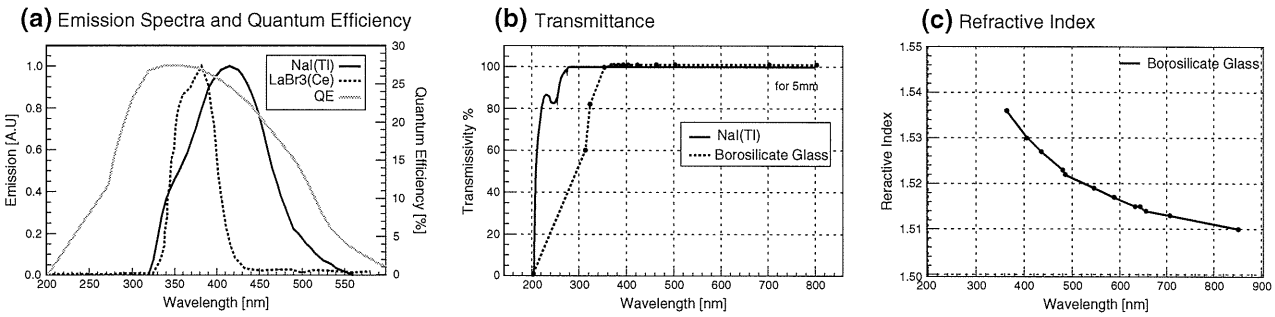

Fig. 2 **a** Emission spectra of NaI(Tl) (*solid line*) and $LaBr_3$(Ce) (*dotted line*) (BrilLanCe350: Saint-gobain) together with the quantum efficiency of the H8500 (*gray line*). **b** Transmittance of NaI(Tl) and borosilicate glass (assumed BK7: Schott Glass). **c** Refractive index of borosilicate glass. These data are available from each specification

surface of the scintillator was covered with a white diffuse reflector. The thickness of the scintillator was varied (10, 8, 6, 4, 2, and 1 mm) and the optical window thickness was also varied (1 and 3 mm). Simulation was also carried out using NaI(Tl) instead of $LaBr_3$(Ce) as the reference. Additional simulations were performed to evaluate effects of varying incident angle for a detector fitted with a pinhole collimator. Finally, detection efficiency defined as follows was estimated

$$\text{Efficency} = \frac{\text{Number of full energy despitions}}{\text{Number of incident gamma rays}}.$$

Densities of NaI(Tl) and $LaBr_3$(Ce) were 3.67 and 5.08 g/cm^3, respectively.

Gamma rays (141 keV) entered the scintillator vertically at 49 positions on a 7 × 7 grid with 15 mm intervals, similar to the source position of the large-FOV detector. In the pinhole configuration, gamma rays were generated at a point 86.6 mm above the center of the detector to the 49 positions. The maximum incident angle was 60°. 1000 gamma rays were simulated at each position.

Analysis

In both the simulation and experiment, the spatial and energy resolutions were evaluated at every grid points as follows. Photo-peak of 141 keV was fitted using a Gauss function, and 3-sigma region as an energy window (e.g., 116–164 keV for the experiment with NaI(Tl)) was selected. Using energy-selected events, interacting points were reconstructed by Anger logic and projected into the x and y directions. The spatial resolution was calculated by fitting with a function that took into account the diameter of holes, expressed as follows:

$$f(x) = \int g(x) \times h(z-x)\mathrm{d}x = \frac{1}{2a}\left\{\mathrm{erf}\left(\frac{a+b-x}{\sqrt{2}\sigma}\right) - \mathrm{erf}\left(\frac{b-x}{\sqrt{2}\sigma}\right)\right\},$$

$f(x)$ is assumed to be a convolution function of the Gauss function $g(x)$, which serves as a point spread function, and the uniform distribution $h(x)$, which describes the source distribution. erf is an error function, a is the diameter of a hole, and b is the position of a hole. The spatial resolutions for each position were calculated according to the term $\sqrt{8\ln 2} \times \sigma$, where σ is the standard deviation of the Gauss function. Finally, the energy resolution was derived from the energy spectra at each position. In this analysis of the experiment, background counts were subtracted from the experimental data.

We compared spatial resolution (FWHM mm) and energy resolution (FWHM %) with experimental results of the large-FOV detector. The planar image, spatial resolution in x and y direction, energy spectra, and their average resolutions were used for the comparisons. Finally, the small-FOV detector was designed to optimize spatial resolution and detection efficiency.

Results

Validation of simulation code

Planar images of multiple point sources obtained from the experiment and the simulation for the large-FOV detector are shown in Fig. 3. It can be seen that intervals between points are constant around the center, but becomes closer at the edge. The spatial resolution in the x direction along the central line is shown in Fig. 4. The spatial resolutions are almost homogenous around the center but become gradually worse at the edge of the detector in both the simulation and experiment. In the simulation, spatial resolution agreed with the experimental results within approximately 10% at ± 105 mm distance from the center. At the position 10 mm away from the detector edge, the resolutions become relatively worse. The experimental mean resolution, omitting those from the edge, were 3.6 and 3.1 mm in

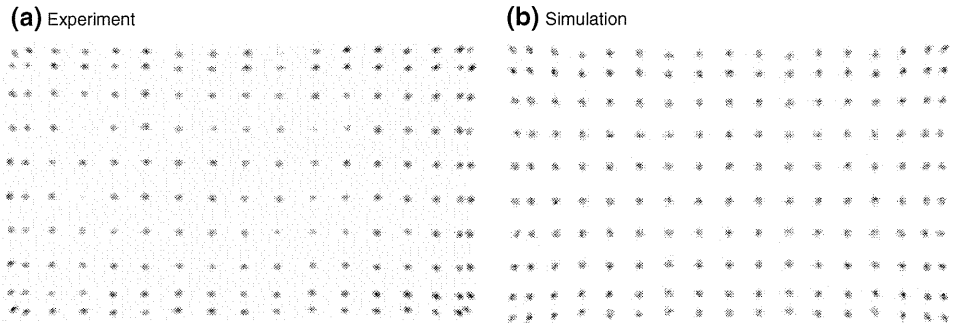

Fig. 3 Planar images of multiple point sources obtained from experiment (**a**) and simulation (**b**). These interacting points are calculated by Anger logic

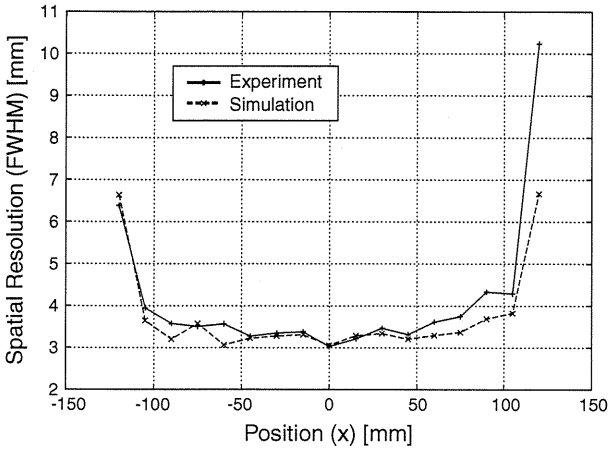

Fig. 4 Comparison of spatial resolutions in the x direction. The resolutions are for lines from the 5th row from the bottom in Fig. 3. The *solid line* shows the experimental result, and the *dotted line* shows the simulation result

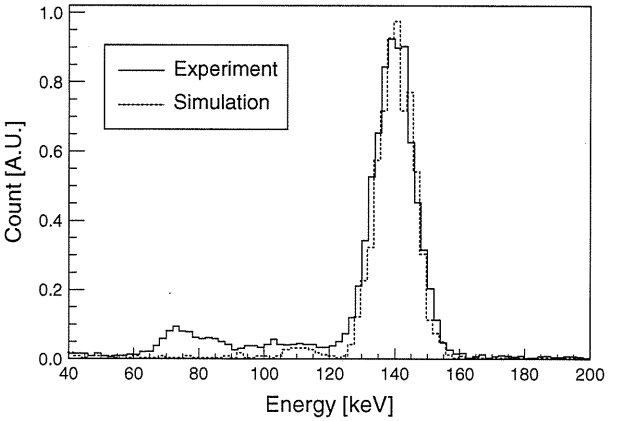

Fig. 5 Energy spectra at the center of the detector. The *solid line* shows experimental results; the *dotted line* shows the simulation. In the simulation, energy spectra are derived from the number of obtained scintillation photons

the x and y directions, respectively. The best resolutions in the x and y directions were 3.0 and 2.7 mm; these were obtained at the center. In the simulation, the mean resolutions in the x and y directions were 3.3 and 3.0 mm, respectively. The best resolutions were 2.8 and 2.6 mm for the x and y directions. Figure 5 shows the energy spectra at the center. The broadness of the peak in the simulation corresponds to the fluctuation of the number of obtained scintillation photons. The energy resolutions determined from spectra of the experiment and the simulation were 10.0 and 9.0% (FWHM), respectively. With respect to energy resolution, clear position dependence was not observed. The mean and deviation of energy resolution of the experiment and the simulation, respectively, were 10.3 ± 0.2 and 9.3 ± 0.3%.

Application of the simulation code for designing high-resolution detector

The simulation results of planar images of multiple point sources for the small-FOV detector with different thicknesses (10, 6 and 1 mm) are shown in Fig. 6. Clear separation of source positions was obtained in the thin scintillator, especially the 1 mm thickness. As the scintillator was thicker, interval of source positions decreased and the point spread function blurred. The mean spatial resolutions with thicknesses of 10, 8, 6, 4, 2, and 1 mm are shown in Fig. 7a together with the cases in which the scintillator is NaI(Tl), the thickness of the optical window is 1 or 3 mm, and the angle of incidence is oblique. In these configurations, comparable resolutions in the x and y directions were obtained. $LaBr_3$(Ce) had better spatial resolution than NaI(Tl) by 22–36%. The best resolution was 0.76 mm with 1 mm thickness. Energy spectra obtained from $LaBr_3$(Ce) and NaI(Tl) of 1 mm thickness at the center of the detector were shown in Fig. 8. The numbers of obtained scintillation photons in an event of full energy deposition (141 keV) were 5039 and 3103, resulting in energy resolution of 8.65 and 11.7%, respectively. The detection efficiencies are shown in Fig. 7b. The maximum efficiency for the 141 keV gamma rays was 93% with 10 mm thickness. The efficiency decreased with thinner scintillator (26% for 1 mm thickness). Varying the optical window between 1 and 3 mm had little effect. For the oblique incident cases, the spatial resolution became slightly worse by several percent.

Figure 9 shows an average distribution of scintillation photons on the 16 × 16 anodes in the case of 1000 gamma rays entering the of the detector. The thicker scintillator has a wider spread of scintillation photons.

Discussion

Adequacy of the simulation

This study demonstrates the adequacy of the simulation code. Both the spatial resolution and the energy resolution appeared to be well reproduced between simulation and experimental data. It has thus been suggested that Geant4 with optical photon processes would be of use when one intends to optimize the design of a new scintillation detector assembly. However, the simulation systematically exhibited small but significant overestimations compared with the experimental data. This can probably be attributed to additional errors in the experiments, which have not been taken into account in the simulation. Potentially influential factors include electrical noise and/or uncertainties in the multiplying processes of the PMTs. The angular

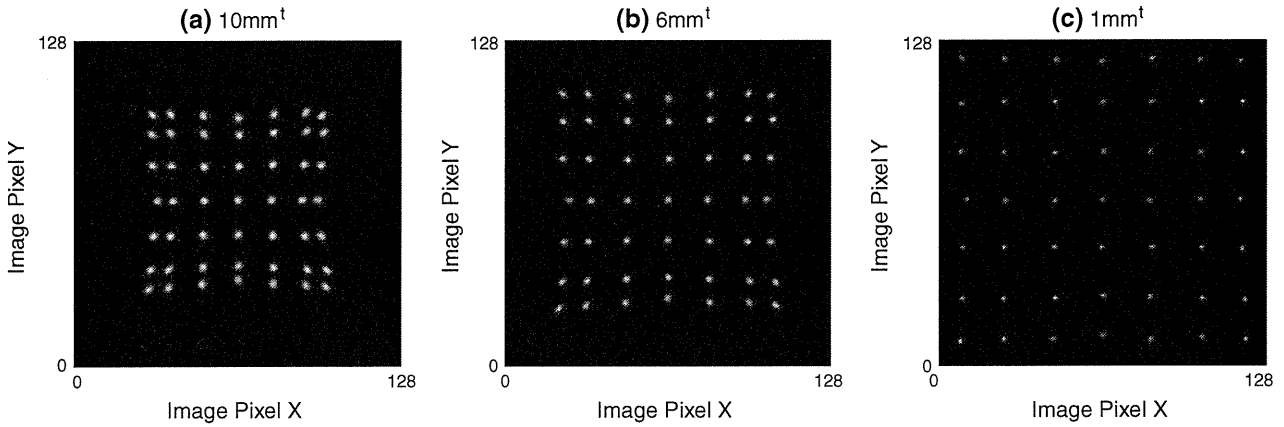

Fig. 6 Reconstruction of interacting points with a simulated $LaBr_3(Ce)$ scintillator with thickness 10 mm (**a**), 6 mm (**b**), or 1 mm (**c**). 141 keV gamma rays entered the $LaBr_3(Ce)$ scintillator vertically at 49 positions arranged in a 7 × 7 grid pattern with 15 mm intervals. Thinner scintillators have better spatial resolutions. Good separations and position linearity were obtained with a 1-mm thickness

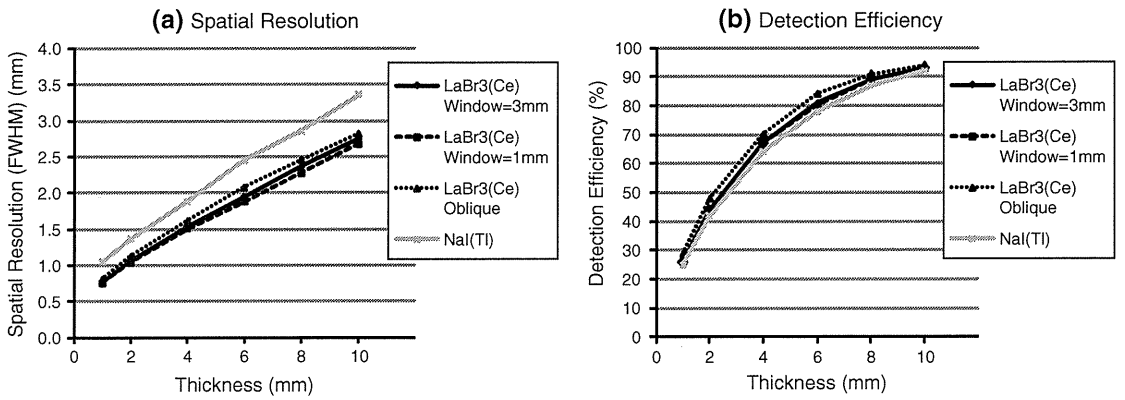

Fig. 7 Spatial resolutions (FWHM, mm) and detection efficiency (%) of the small-FOV detector estimated by simulation. Thickness was varied from 10 to 1 mm."OpWin" stands for the optical window. "Oblique" means that gamma rays enter the scintillator at an oblique angle

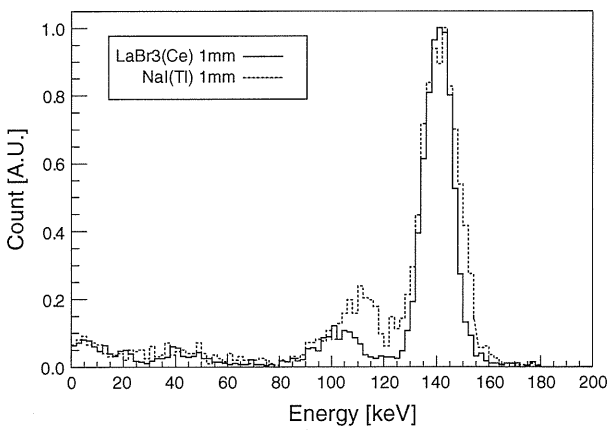

Fig. 8 Energy spectra $LaBr_3(Ce)$ (*solid line*) and NaI(Tl) (*dot line*) of 1 mm thickness at the center of the small FOV detector normalized by the maximum counts. Energy resolutions of $LaBr_3(Ce)$ and NaI(Tl) were 8.65 and 11.7%, respectively

distribution of the source is also considered as an influential factor. The beam was parallel in the simulation, but there were slight obliquely incidents in the experiment. Differences in the spatial resolution in the x and y directions can be attributed to difference of the number of cathodes along the x and y axes. The larger number of cathodes causes a larger uncertainty in the position identification due to the statistical fluctuation of scintillation photons at each anode. Note that the simulation of a square detector geometry for the small-FOV detector resulted in comparable resolutions for both the x and y directions. The spatial resolution has a position dependency, and decreases near the edge. This is because the distribution of the scintillation photons entering the cathodes is isotropic at the center, while scintillation photons partially reflect at the edge, resulting in an asymmetrical distribution at the edge of the detector. This caused decreased linearity performance and degraded spatial

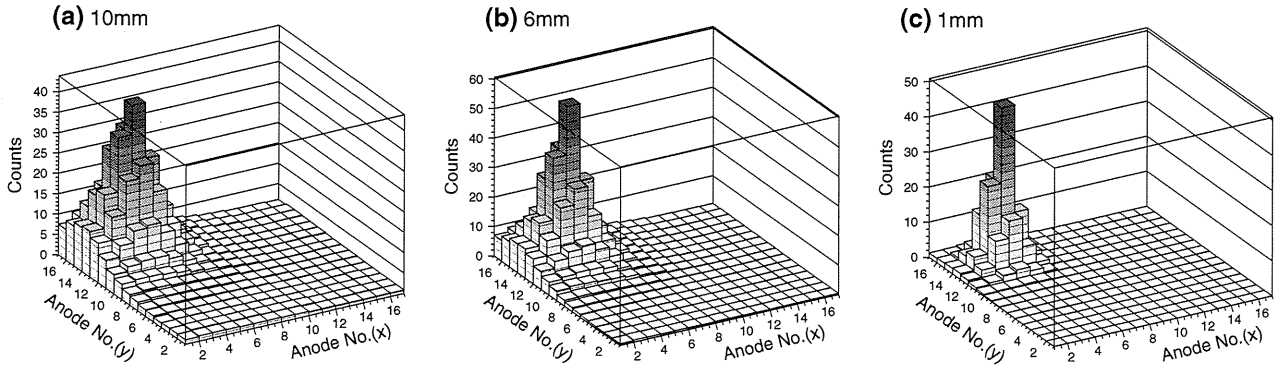

Fig. 9 Average distribution of scintillation photons on the 16 × 16 array of anodes. Gamma rays enter the edge of the detector. Scintillator thickness is 10 mm (**a**), 6 mm (**b**), or 1 mm (**c**)

resolution near the edge. Energy resolution depends on the number of observed scintillation photons. Homogeneous energy resolution indicates that the correction efficiencies of scintillation photons are almost equal over the entire detector. Importantly, the energy resolution was highly reproducible without any arbitrary parameters. It is often the case in most Monte Carlo simulation studies that energy resolution is fitted to match the experimental results. However, this simulation can reproduce the energy resolutions for a given set of detector design parameters. This is one of the most important features of this study. The simulated energy spectrum of the scatter region (below 120 keV) was different from the experimental results. It was probably due to the scatter from the collimator in the experiment. The simulation did not include interaction with the collimator.

Conceptual design of high-resolution SPECT system for human brain

We performed the simulation for optimizing a new high-resolution detector system for SPECT described in [9]. A pinhole collimator can be adopted to achieve the high spatial resolution typically achieved with a small-FOV. The reconstructed FOV can, however, be truncated if applied to an object which is larger than the FOV; this truncation can cause artifacts in the reconstructed images, and errors in the quantitative pixel counts. A new technique for truncation-compensated 3D-OSEM reconstruction [11], based on the theory proposed by Kudo et al. [12], could be one application of the two detectors presented in this study. One detector, with an NaI(Tl)-based large-FOV detector, provides an image without truncation, and is used as a supporting information for reconstructing truncated data from the small-FOV detector successfully. The small-FOV detector has the potential to provide high resolution of approximately 1 mm, but with possible truncation. Thus, the combination of the two types of detectors may provide SPECT images with both high spatial resolution and the quantitative accuracy of a magnified FOV. To achieve such a high resolution in practice, a prior high-accuracy estimate is essential. Monte Carlo simulation code, validated for a scintillator based on multi-anode PMTs, would be helpful for optimizing and validating various design configurations.

Design of the small-FOV detector with high resolution

$LaBr_3(Ce)$ is a promising material for use in scintillator crystals to achieve higher resolution than NaI(Tl); this is primarily due to the larger amount of scintillation photons, as demonstrated in this study. The thinner scintillator provides better spatial resolution, because thinner scintillators prevent the spread of scintillation photons, as shown in Figs. 6, 7 and 9. However, efficiency decreases with a thinner scintillator crystal, resulting in reduced sensitivity of gamma-ray detection. Thus, there is a trade-off between spatial resolution and detection efficiency. A thickness of 6 mm appeared to be best suited for our detector system, as we originally aimed at achieving a spatial resolution $\sim$1 mm with sufficient detection efficiency. If we use a pinhole collimator with 0.5 mm diameter and threefold magnification factor, an intrinsic spatial resolution of $\sim$2 mm would provide the spatial resolution of 1 mm in a SPECT system [13]. The simulation demonstrated that a 6 mm thickness of $LaBr_3(Ce)$ can provide $\sim$2 mm intrinsic spatial resolution and a detection efficiency of approximately 86% for Tc-99m, that efficiency is comparable to the performance of currently popular SPECT detectors. Using a pinhole collimator, spatial resolution could be slightly worse; this would be attributed to the spread of interaction points in the x–y plane due to the oblique angle of incidence. To evaluate the differences between vertical and oblique angles of incidence, it is necessary to simulate both gamma rays and scintillation photons, as we have done in this simulation study. Geant4 is of use for such evaluations, because it takes both processes into account.

Detector systems that consist of a monolithic scintillator and multi-anode PMTs have the potential to improve spatial resolution over what is currently achievable. In this study, Anger logic using all anodes was employed to identify an interacting point. Anger logic using a subset of anodes will improve the spatial resolution, the nearest-neighbor algorithm [14], and nonlinear least squares method [15] are also promising methods. In the future, in order to employ these methods, analog-to-digital converters (ADC) for all anodes will be installed in our detector systems.

Conclusion

We performed the Geant4 simulation that took into account propagation of gamma rays and transport of scintillation photons. The simulation reproduced experimental results with regard to both spatial resolution and energy resolution for a SPECT detector based on NaI(Tl) scintillator and position sensitive PMTs (H8500). We demonstrated a simulation for a design of the small-FOV detector to optimize geometrical parameter. This simulation may be useful to provide an optimal design of a SPECT detector without physical experiments.

Acknowledgments The authors would like to thank Mr. Hiroyuki Mashino of EspecTecno Corporation, Kobe, Japan, for his skillful assistance with an acquisition system of the detector. This work was supported in part by the Project from Kansai Bureau of Economy, Trade and Industry of Japan; a Grant for Research on Health Labour Sciences Research Grant, from the Ministry of Health, Labour and Welfare (MHLW) of Japan; the Budget for Nuclear Research of the Ministry of Education, Culture, Sports, Science and Technology (MEXT) of Japan; and the Grant-in-Aid for Scientific Research from MEXT of Japan.

References

1. Agostinelli S, Allison J, Amako K, Apostolakis J, Araujo H, Arce P, et al. GEANT4 a simulation toolkit. Nucl Instrum Methods Phys Res A. 2003;506:250–303.
2. Van Der Laan DJ, Dennis RS, Maas MC, Beekman FJ, Bruyndonckx P, van Eijk CWE. Optical simulation of monolithic scintillator detectors using GATE/GEANT4. Phys Med Biol. 2010;55:1659–75.
3. Sergio LM, Giuseppe B, Paolo B, Dante B, Valentino OC, et al. Optical physics of scintillation imagers by GEANT4 simulations. Nucl Instrum Methods Phys Res A. 2009;607:259–60.
4. Ciocia F, Braem A, Chesi E, Leo RD, Joram C, Lagamba L, et al. GEANT4 studies on the propagation and detection of scintillation light in long thin YAP crystals. Nucl Instrum Methods Phys Res A. 3009;600:506–12.
5. Wirth S, Metzger W, Pham-Gia K, Heismann BJ. Impact of photon transport properties on the detection efficiency of scintillator arrays. IEEE Nuclear Sci Symp Confer Record. 2006; 2602–3
6. Soreefan AM, Hui T, DeVol TA, Dept. Experimental and monte carlo investigation of the light collection efficiency of heterogenous scintillation flow cell detectors. IEEE Nuclear Sci Symp Confer Record. 2003;760–2
7. Pani R, Pellegrini R, Cinti MN, Bennatia P, Bettia M, Vittorinia F, et al. LaBr3:Ce crystal: the latest advance for scintillation cameras. Nucl Instrum Methods Phys Res A. 2007;572:268–9.
8. Pani R, Cinti MN, Pellegrinia R, Bennatia P, Bettia M, Vittorinia F, et al. LaBr3:Ce scintillation gamma camera prototype for X and gamma ray imaging. Nucl Instrum Methods Phys Res A. 2007;576:15–8.
9. Zeniya T, Hirano Y, Sakimoto T, Ishida K, Watabe H, Teramoto T, et al. Conceptual design of high resolution and a quantitative SPECT system for imaging a selected small ROI of human brain. IEEE Nuclear Sci Symp Confer Record. 2009; 3484–6
10. Li C, Wang B, Wang R, Wang H, Zhu Z. First-principles study of the electronic and optical properties of lanthanide bromide. Thin Solid Films. 2008;516:7894–8.
11. Zeniya T, Watabe H, Inomata T, Iida H, A Sohlberg, H Kudo. 3DOSEM reconstruction from truncated data in pinhole SPECT. IEEE Nuclear Sci Symp Confer Record. 2007; 4205–7
12. Kudo H, Courdurier M, Noo F, Defrise M. Tiny a prior knowledge solves the interior problem in computed tomography. Phys Med Biol. 2008;53:2207–31.
13. Jaszczak RJ, Li J, Wang H, Zalutsky MR, Coleman RE. Pinhole collimation for ultra-high-resolution small-field-of-view SPECT. Phys Med Biol. 1994;39:425–37.
14. Maas MC, Schaart DR, Van Der Laan DJ, Bruyndonckx P, Lemaitre C, Beekman FJ, et al. Monolithic scintillator PET detectors with intrinsic depth-of-interaction correction. Phys Med Biol. 2009;54:1893–908.
15. Zhi Li, Wedrowski M, Bruyndonckx P, Vandersteen G. Nonlinear least-squares modeling of 3D interaction position in a monolithic scintillator block. Phys Med Biol. 2010;55:6515–32.

Journal of Molecular Spectroscopy 274 (2012) 14–21

Contents lists available at SciVerse ScienceDirect

Journal of Molecular Spectroscopy

journal homepage: www.elsevier.com/locate/jms

Determination of two-photon-excitation cross section for molecular isotope separation

A. Wakai [a], K. Tsuchida [c], T. Fukumura [a,*], H. Iida [b], K. Suzuki [a]

[a] Department of Molecular Probes, Molecular Imaging Center, National Institute of Radiological Sciences, 4-9-1 Anagawa, Inage-ku, Chiba 263-8555, Japan
[b] Department of Bio-medical Imaging, National Cerebral and Cardiovascular Center Research Institute, 5-7-1 Fujishirodai, Suita-shi, Oosaka-fu 565-8565, Japan
[c] Medical System and Nuclear Equipment Division, Hitachi Works, Power Systems, Hitachi, Ltd., 1-1, Saiwai-cho, 3-chome, Hitachi-shi, Ibaraki-ken 317-8511, Japan

ARTICLE INFO

Article history:
Received 16 February 2012
Available online 28 March 2012

Keywords:
Elimination method
REMPI
C state
Molecular dissociation
A state
PET

ABSTRACT

We observed that the two-photon excitation of a ν_3 hot band (6*s* Rydberg $3;3_1^0$) in methyl iodide is promising for isotopic laser separation, because the isotope shift of the multiphoton ionization (MPI) resonance is resolvable. To estimate the excitation cross section, which gives the enrichment factor (final isotope ratio per initial isotope ratio) of the separation method, we devised a method based on a pump–probe MPI procedure. By probing the material remaining after irradiation with the pump pulse, we estimated the cross section of the ground-state transition (6*s* Rydberg 3;0–0) to be $4.1 \pm 1.4 \times 10^{-48}$ (cm^4 s). The enrichment factor predicted from this cross section indicates that a high-performance laser system (20 mJ/pulse, 200 Hz, 10 ns duration) was capable of achieving an enrichment of over 1000-fold in view of the dissociation efficiency under low-pressure gas conditions. Thus, laser separation (elimination) appears to be a promising tool to create positron-emission tomography molecular probes.

1. Introduction

An important theme in the use of positron-emission tomography (PET) has been to improve the specific activity (SA), which defined as the amount of radioactivity per unit mass of labeled compound [1]. Although ^{11}C-methyl iodide is a versatile precursor for ^{11}C-labeled molecular probes [2–4], it is contaminated during its synthesis by stable carbon isotopes, which reduces the SA [5–7] of the subsequent ^{11}C-labeled molecular probes. ^{11}C is usually diluted by three to four orders of magnitude below the level theoretically necessary. If a high-purity labeled compound could be obtained with the requisite SA, it would lead to a new and widespread use of PET technology [8]: for instance, to image new low-density receptors [9,10]. In working toward this goal, a chemical approach [10] obtained an order of magnitude (or more) increase in SA, but this corresponds to only 1/70 of the theoretically necessary level and appears to be close to the upper limit for the approach. Thus, a new approach is required.

Isotopic-enrichment techniques, especially UV laser separation [11,12] by isotopic molecular dissociation, can serve to increase the SA of labeled compounds, but they require an isotopically resolvable resonance. The two-photon excitation of the 6*s* Rydberg $3;3_1^0$ transition [13], which we found by resonance-enhanced multiphoton ionization (REMPI) of CH_3I to be isotopically resolvable [14], is a good candidate for UV separation. In what follows, we use the nomenclature of Felps et al. [15]. However, this transition is two-photon allowed and single-photon suppressed [13,16], and the cross section of two-photon excitation is extremely small in comparison with the cross section for single-photon excitation [17]. Thus, we focused our attention on studying the cross section of this excitation, which along with the laser characteristics, determines the performance of the laser separation method. However, no reports exist concerning this excitation cross section. In general, two-photon-excitation cross sections of molecules are measured by transmission methods such as Z-scan [18] techniques, two-photon-induced fluorescence [19,20], or ion-yield curve fitting based on rate equations [21]. However, these techniques are not suitable for CH_3I in low-pressure gas conditions because it dissociates without fluorescence from its excited state to fragments.

Therefore, we devised a method based on pump–probe multiphoton ionization (MPI) [22,23] and measured the excitation cross section of the relevant ground-state transition (6*s* Rydberg 3;0–0). Furthermore, we estimated the enrichment factor (final isotope ratio per initial isotope ratio) by a UV laser system from the obtained cross section. In the pump–probe MPI scheme, the probe normally selectively excites or ionizes either a product or the excited reactant, which is produced by the pump pulse. Examples of this approach include excited-state-dynamics studies [24], excited-state-lifetime measurements [25–27], fragment kinetics studies [28,29], or measurements of fragment population after dissociation [30]. However, in our method, the probe pulse is used to estimate

* Corresponding author. Fax: +81 43 206 3261.
E-mail address: t_fukumu@nirs.go.jp (T. Fukumura).

0022-2852/$ - see front matter © 2012 Elsevier Inc. All rights reserved.
http://dx.doi.org/10.1016/j.jms.2012.03.004